Pressure-driven configurational crossover between $4f^7$ and $4f^65d^1$ States – Giant enhancement of narrow Eu^{2+} UV-Emission lines in SrB_4O_7 for luminescence manometry

Teng Zheng [a], Marcin Runowski [a,f,*], Plácida Rodríguez-Hernández [b], Alfonso Muñoz [b], Francisco J. Manjón [c], Małgorzata Sójka [d], Markus Suta [e], Eugeniusz Zych [d], Stefan Lis [a], Víctor Lavín [f,*]

[a] *Adam Mickiewicz University, Faculty of Chemistry, Uniwersytetu Poznańskiego 8, 61-614 Poznań, Poland*
[b] *Departamento de Física, MALTA Consolider Team, and Instituto de Materiales y Nanotecnología, Universidad de La Laguna, Apartado de Correos 456, E-38200 San Cristóbal de La Laguna, Santa Cruz de Tenerife, Spain*
[c] *Instituto de Diseño para la Fabricación y Producción Automatizada, and MALTA Consolider Team, E.T.S. Ingeniería del Diseño, Universitat Politècnica de València, Cno. de Vera s/n, 46022 València, Spain.*
[d] *University of Wrocław, Faculty of Chemistry, F. Joliot-Curie 14, 50-383 Wrocław*
[e] *Inorganic Photoactive Materials, Institute of Inorganic Chemistry, Heinrich Heine University Düsseldorf, Universitätsstr. 1, D-40225 Düsseldorf, Germany*
[f] *Departamento de Física, MALTA Consolider Team, and IUdEA, Universidad de La Laguna, Apartado de Correos 456, E-38200 San Cristóbal de La Laguna, Santa Cruz de Tenerife, Spain*

ARTICLE INFO

ABSTRACT

Accurate, fast, and non-invasive methods for the determination of the local pressure magnitude are crucial for the investigation of the physical and chemical behavior of materials at the extreme conditions of high pressure. A promising method for remote *operando* pressure measurements is luminescence manometry. However, a limiting bottleneck for high-pressure readout is the usually occurring quenching of the emission signal of the luminescent sensor material upon compression. In this work, we reported for the first time the pressure-induced intensity enhancement (by 3 orders of magnitude) of the $4f^7(^6P_{7/2}) \to 4f^7$ ($^8S_{7/2}$) emission line of Eu^{2+} in the UV range due to pressure-induced configurational crossover between the excited $4f^65d^1$ and $4f^7$ energy levels in SrB_4O_7 host. The peak centroid of the narrow $4f^7 \to 4f^7$ transition exhibits a significant red-shift ($\sim$ -12.84 cm^{-1} GPa^{-1}; 0.17 nm GPa^{-1}) with simultaneous temperature independence of the line position (4.8·10^{-4} nm K^{-1}). The pressure sensitivity of the proposed system is competitive to the so far well-established luminescent pressure sensors based on Al_2O_3:Cr^{3+} (ruby) and SrB_4O_7:Sm^{2+} with characteristic narrow line emission in the red range, and offers an alternative spectral range in parallel with an intensity enhancement at higher pressures. This novel pressure gauge may significantly improve the accuracy of the remote pressure measurements and open up new horizons for materials science research at even higher pressures.

© 2022 Acta Materialia Inc. Published by Elsevier Ltd. All rights reserved.

1. Introduction

In recent decades, the implementation of high pressure (HP) in scientific research in many laboratories worldwide led to the discovery of new phenomena, *e.g.,* phase transformations and formation of new materials, as well as an in-depth insight into the intriguing and conclusive mechanisms that have generated great progress in solid-state physics/chemistry, material science, and geophysics [1–3]. In response to external mechanical stimuli such as pressure, considerable changes occur in the material related to a change in the interatomic distances [4], alteration of electronic orbitals [5], *etc* [6,7]. These changes are usually accompanied by alterations in the nature of the chemical bonds and coordination numbers thus leading to other structure types with different electronic properties at HP [8–12]. In this context, the fast and precise monitoring of the locally present pressure is of utmost importance.

In order to precisely monitor pressure values at HP conditions in laboratory and industrial processes, optical pressure gauges, typically based on Cr^{3+} (mostly ruby; Al_2O_3:Cr^{3+}) and various lanthanide-doped (mostly Sm^{2+}) materials, have gained great attention, mainly due to their low electronic noise, rapid and non-

---

invasive detection and chemical durability [13–15]. Most of the established luminescent pressure sensors, including the two previous examples, emit in the red or near infrared range. However, there is still a bottleneck in experimental pressure-sensing techniques based on photoluminescence to significantly improve the accuracy of pressure measurements and widen the pressure sensing range covered by these techniques. The bottleneck is the ubiquitous and progressive compression-induced quenching of emission of lanthanide ($Ln^{3+/2+}$) and transition metal ions (including Cr^{3+} in ruby) accommodated in a host lattice. To the best of our knowledge, this is a notoriously observed effect in all luminescence pressure sensors reported so far [4,16,17].

Among other Ln^{2+} ions, the divalent europium ion (Eu^{2+}) is particularly attractive for its important role in light-emitting diodes (LED) and optical displays, due to its largely tunable, broad $4f^6 5d \leftrightarrow 4f^7$ emission band leading to good color rendering properties. The high sensitivity of the 5d orbitals to the nature of the chemical bond to the surrounding ligands in a host compound makes the photoluminescence of Eu^{2+} highly tunable [18–20] with known examples for emission in the UV-violet [21], blue [22], red [23], and even NIR regions depending on the host matrix [23–27]. Aside from that, the emission of Eu^{2+} associated with the alternatively possible intra-configurational $4f^7$ ($^6P_{7/2}$)$\rightarrow 4f^7$ ($^8S_{7/2}$) transitions characterized by several sharp, narrow ($\approx$ 1-2 nm width in the wavelength domain) emission lines in the UV range at around 360 nm is only occasionally reported and typically observed in highly ionic host compounds [28–30]. Understanding the control mechanisms of the appearance of this unusual type of luminescence of Eu^{2+} is not only relevant from a fundamental perspective but also important for potential industrial applications [18–23].

Borates, which are naturally deposited in the sediments of ancient lakes or in hydrothermal solutions in the products of the hervidero hotbed, play an irreplaceable role in industrial and scientific fields [31]. Strontium tetraborate (SrB_4O_7) is a well-known material in non-linear optics and luminescence pressure sensing. Its superiority lies mainly in its high non-linear optical coefficients, high optical damage thresholds, neutron sensitivity, wide optical transparency in the UV-vacuum range, with the fundamental absorption edge below 120 nm ($\sim$83 333 cm^{-1}), that extends towards $\sim$ 3250 nm ($\sim$ 3077 cm^{-1}) in the IR range [32–35]. Due to the rigid three-dimensional network of the corner-linked tetrahedral $(BO_4)^{5-}$ anion structure groups of the boron-oxygen framework, SrB_4O_7 shows excellent stabilization of the divalent lanthanide ions even in air [21]. Huppertz *et al.* reported a HP β-CaB_4O_7 phase, which crystallizes isotypically to SrB_4O_7 in the space group $Pnm2_1$ (no. 31) [36]. Upon doping of Eu^{2+} ions into the SrB_4O_7 crystal structure, Machida *et al.* observed a very efficient broad luminescence band at around 367 nm at room temperature (RT), which is assigned to the $4f^6 5d \rightarrow 4f^7 (^8S_{7/2})$ transition of Eu^{2+} [37]. On the other hand, Meijerink *et al.* observed sharp lines caused by the transitions within the $4f^7$ ground configuration at low temperatures [38] and showed that a configuration crossover between the $4f^7$ and $4f^6 5d^1$ configuration of Eu^{2+} can be stimulated by temperature variation, which was confirmed by some of us recently [33]. However, detailed HP studies of Eu^{2+}-doped SrB_4O_7 have never been performed before and offer additional insights into this configuration crossover and its potential use for remote sensing applications.

In this work, we regard the influence of high pressure on the photoluminescence properties of Eu^{2+} in SrB_4O_7. Moreover, we consider the potential of SrB_4O_7 for applications at higher pressures by evaluation of the elastic and mechanical properties of this compound. For that purpose, we performed density functional theory (DFT) calculations under periodic boundary conditions and related the computational results to vibrational spectra at varying pressure. We observed a so far not reported pressure-induced enhancement of the narrow $4f^7$ ($^6P_{7/2}$) $\rightarrow$ $4f^7$ ($^8S_{7/2}$) emission lines of Eu^{2+}, exhibiting a linear red-shift of $\sim$ -12.84 cm^{-1} GPa^{-1} ($\sim$ 0.17 nm GPa^{-1}) within the pressure range of $\sim$ 0 - 60 GPa. The observed pressure-induced enhancement of the emission is beneficial for applications as a pressure gauge, as the UV emission of Eu^{2+} doped into SrB_4O_7 is robust towards quenching effects. Moreover, it does not interfere with the luminescence of most conventional phosphors upon usage as an internal pressure sensor. Overall, the investigation of the pressure-dependent luminescence properties of SrB_4O_7:Eu^{2+} could offer a first step towards the development of an alternative concept in sensitive luminescence manometry.

2. Experimental

2.1. Synthesis and characterization at ambient condition

Details of the synthesis protocol, structural and spectroscopic characterization including X-ray diffraction (XRD) patterns, scanning electronic microscopy (SEM), energy dispersive X-ray (EDX) analysis, as well as luminescence spectroscopy studies at ambient conditions of the SrB_4O_7: Eu^{2+}, Sm^{2+} samples can be found in our previous work [39].

2.2. DAC loading procedure

For high-pressure measurements, we applied a typical Merrill-Bassett diamond anvil cell (DAC), equipped with high-purity IIas diamond anvils (for Raman and fluorescence spectroscopy), purchased from Almax easyLab. The pressure values inside the DAC chamber are adjusted with three metal screws. Stainless-steel sheets (thickness: 250 µm) with an aperture of $\sim$150 µm (hole size) were applied as gaskets, used for high-pressure experiments in DAC. Before loading the sample, the gaskets were pre-indented down to $\sim$80 µm (sample thickness). Using a stereo microscope, the sample and a single ruby ball ($<$ 10 µm diameter) was loaded into the DAC chamber, and, subsequently the pressure transmitting medium composed of a solvent system of methanol/ethanol/water (at a volume ratio 16:3:1) was filled in the DAC chamber for maintaining hydrostatic and quasi-hydrostatic conditions during the compression process.

2.3. High-pressure Raman scattering characterization

Raman spectra were recorded in backscattering geometry with a Renishaw InVia confocal micro-Raman system, using a grating with 1800 grooves/mm and a power-controlled 785 nm laser diode. The laser beam was focused using an Olympus x20 SLMPlan N long working distance objective.

2.4. High-pressure Photoluminescence characterization

The photoluminescence characterization at high pressure conditions was performed by measuring the emission spectra (with a resolution of $\approx$0.1 nm) of the samples placed in the DAC chamber, using an Andor Shamrock 500i spectrometer, equipped with a detector of iDus 420 CCD camera. The applied excitation light source was a 280 nm UV diode, which was focused on the sample in the gasket hole of DAC. The photoluminescence signal was collected in an optimized configuration with 180° detection geometry (back illuminated configuration). The pressure calibration of the system in the DAC chamber was based on the monitored shift of the ruby R_1 fluorescence line, using the standard ruby calibration curve from http://kantor.50webs.com/ruby.htm.

2.5. Low-temperature Photoluminescence characterization

Low-temperature photoluminescence characterization was performed using an FLS1000 Fluorescence spectrometer (Edinburgh Instruments Ltd) with a 450-W xenon arc lamp (excitation light source) and a Hamamatsu R928P high-gain photomultiplier (cooled -20°C). Emission spectra were collected in the temperature range of 11 – 300 K, with a 10 K step. The decay curves were recorded using an EPLED285 (285 nm) picosecond pulsed light-emitting diode and the same FLS1000 spectrometer. The sample for low-temperature measurements was mounted on a Cu-holder of a closed-cycle helium cryostat (Lake Shore Cryotronics, Inc.) using Silver Adhesive 503 (Electron Microscopy Sciences).

3. Overview of the calculations

Ab initio simulations of bulk SrB_4O_7 were performed within the framework of DFT [40], as implemented in the Vienna Simulation package (VASP) [41]. The projector-augmented wave pseudopotential (PAW) [42] was employed to describe the atomic species. Due to the presence of oxygen atoms, a plane-wave energy cut-off of 540 eV was used to obtain accurate results. The exchange-correlation energy was described within the generalized gradient approximation (GGA) with the Perdew-Burke-Ernzenhof prescription for solids (PBEsol) [43]. Integrations over the Brillouin zone (BZ) were carried out with ($6\times6\times2$) meshes of Monkhorst-Pack special k-points [44]. Thanks to this procedure, the convergence achieved in the energy was better than 1 meV per formula unit and for a set of selected volumes, the cell parameters, and atomic positions were fully optimized by calculating the forces on atoms and the stress tensor. In the optimized configurations, the forces on atoms were less than 0.002 eV/ Å and the deviation of stress tensor components from the diagonal hydrostatic form - lower than 0.1 GPa. For completeness, electronic band structure calculations were carried out along high-symmetry directions in the first Brillouin zone.

The direct force-constant method was employed to study the lattice vibrations, which is available in http://wolf.ifj.edu.pl/phonon. Lattice dynamic calculations were carried out under pressure at the zone center (Γ point) of the BZ. These calculations also allow identifying the symmetry and eigenvectors of the vibration modes of the considered structures at the Γ point. The supercell method was used to obtain the phonon dispersion and the projected phonon density of states (DOS) using a ($2\times2\times2$) supercell.

The elastic constants were evaluated by computing the macroscopic stress for a small strain applying the stress theorem [45,46], as implemented in the VASP code [47]. The mechanical stability and elastic properties of SrB_4O_7 were also studied, since the elastic moduli can be obtained from the calculated elastic stiffness constants.

4. Results and discussion

4.1. Properties at ambient conditions

4.1.1. Structural properties

All details about the conducted experiments are presented in the supporting information (SI) file. As shown in **Fig. S1a-c** in SI, the emission bands of both the $4f^65d\leftrightarrow4f^7$ and $4f^7\rightarrow4f^7$ transitions of Eu^{2+} are clearly observed in the UV range of the emission spectra of SrB_4O_7:0.01Eu^{2+} (without Sm^{2+}) and SrB_4O_7: $x$$Eu^{2+}$, 0.01$Sm^{2+}$ (x=0.005, 0.01, 0.03, 0.05, 0.07 and 0.09) materials. The presence of a small amount of Sm^{2+} ions in the phosphors is related to our previous work on the investigation of the pressure sensing performance of Sm^{2+} in these materials in the visible range upon exploitation of an energy transfer from Eu^{2+} ones [39].

The obtained samples are composed of microcrystalline SrB_4O_7 powder that can be synthesized reproducibly [39]. The morphology of the material was checked by SEM at various magnifications, as shown in Figure S2a-c, confirming the phosphor material is composed of micron-sized particles. First, an additional detailed structural analysis of a representative powder sample SrB_4O_7: 0.03Eu^{2+}, 0.01Sm^{2+} was performed here, as this sample shows a strong emission signal. The structure of SrB_4O_7: 0.03Eu^{2+}, 0.01Sm^{2+} was refined with the Rietveld (whole profiled) method based on the experimental powder X-ray diffraction pattern using the structural model according to diffraction data from the ICDD (card. no. 071-2191) as an input (see Fig. 1**a**) [48]. No traces of additional phases are found. It crystallizes in an orthorhombic structure with the space group $Pmn2_1$ (no. 31) and the Rietveld refinement allows obtaining the following cell parameters and unit-cell volume values: a = 10.7148 Å, b = 4.4428 Å, c = 4.2362 Å, V=201.00 Å^3, and a density of 4.055 g•cm^{-3}, with (R_{wp} = 8.59%; R_{exp} = 3.91%; R_p = 6.45%; g_{of} = 2.2). The error for the determined unit cell parameters (a, b and c) is about $\pm$0.0001 Å. These values are comparable with those found for the bulk crystal (a = 10.724 Å, b = 4.447 Å, c = 4.239 Å, and V = 202.16 Å^3) [49] and those obtained from *ab initio* calculations (see **Table S1** in SI). The collected data are even comparable to those found in the stoichiometric EuB_4O_7 crystal, *i.e.*, (a = 10.731 Å, b = 4.435 Å, c = 4.240 Å, and V = 201.8 Å^3) [50], which is considered due to the similar ionic radii between Eu^{2+} and Sr^{2+}. Additionally, the indexed experimental XRD pattern, clearly showing the matching with the reference ICDD pattern (071-2191), is given in Figure S2d.

According to the Krogh–Moe theory [51], the structure of strontium tetraborate is not a random distribution of BO_4 tetrahedra. Instead, these units are assembled to form well-defined, condensed [B_4O_7] tetraborate groups, building a rigid three-dimensional network with channels parallel to the short crystallographic axes b and c, which leads to the formation of large cavities. All these tetrahedra are distorted and there are two kinds of borate units, [$B(1)O_4$] and [$B(2)O_4$], with mean B-O distances of 1.478 Å and 1.486 Å, respectively. In this structure, four independent positions of the O atoms can be found and they can be divided into two groups: O(1), O(2), and O(3) are linked to two B atoms with shorter B-O bonds ($<$ 1.47 Å), while O(4) is linked to three B atoms with longer B-O bonds ($>$ 1.53 Å). The latter is an original motif within the structure compared to other borates. Consequently, it is characterized by considerably elongated, much weaker bonds, *i.e.*, the average B–O(4) distance is 1.55 Å, while the B–O distances for the remaining oxygen atoms range from 1.36 to 1.47 Å.

There are six-membered B–O rings in the borate network parallel to the b axis. The Sr^{2+} cation occupies large cavities formed by these channels and it has only one crystallographically independent site coordinated by nine oxygen atoms, with distances varying from $\sim$ 2.54 Å to $\sim$ 2.83 Å. This gives rise to a [SrO_9] capped cube nonahedron with C_S local point symmetry. As mentioned above, the real site symmetry on the Sr sites in SrB_4O_7 is C_s. However, for a luminescent ion with extended and diffuse 5d orbitals such as Eu^{2+}, usually the "experienced" site symmetry of the dopant is somewhat higher. Upon regarding the nine-fold coordinated Sr site in SrB_4O_7, eight oxygen ligands form a slightly distorted cube, while the other oxygen ligand is on the tip and lies on a four-fold rotation axis. This allows an effective C_{4v} site symmetry as the approximation for the doped lanthanide ion [52].

It is noteworthy that the BO_4 tetragonal units surround the channel forming a cage that isolates the divalent lanthanide ions, which is usually considered as the reason for the high stability of the otherwise reactive divalent oxidation state of the lanthanides in this structure [53]. In addition, similar ionic radii values for coordination 6, of Eu^{2+}, Sm^{2+} and Sr^{2+} (R(Sr^{2+}) = 1.18 Å; R(Eu^{2+}) = 1.17 Å; R(Sm^{2+}) = 1.17 Å) [54], facilitate the incorpo-
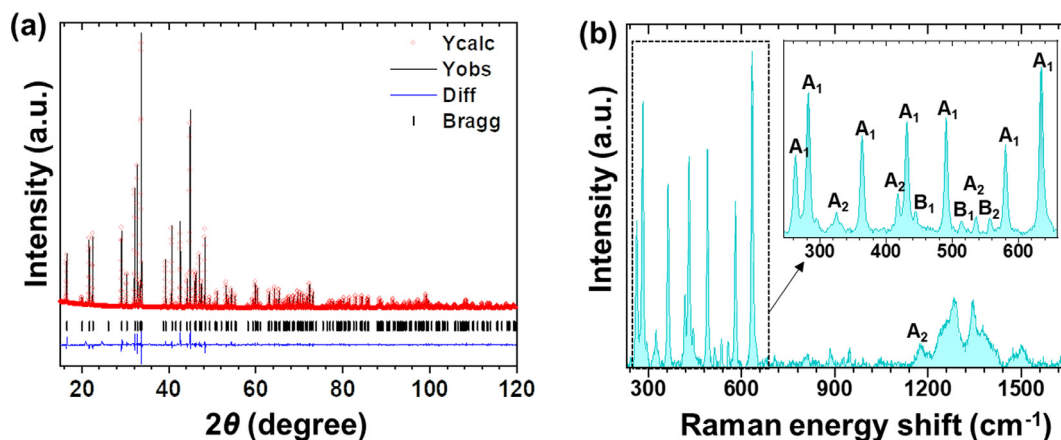
Fig. 1. a) Experimental (black) powder XRD pattern of SrB_4O_7: $0.03Eu^{2+}$, $0.01Sm^{2+}$ and corresponding theoretical (red) XRD pattern. b) Experimental Raman spectrum of the SrB_4O_7: $0.03Eu^{2+}$, $0.01Sm^{2+}$ sample measured at ambient conditions.

ration of the Eu^{2+} and Sm^{2+} into the network substituting Sr^{2+} ions in the nonahedron, without the need for charge compensation [49,50]. Machida *et al.* suggest that the rigid 3D-network of tetrahedral $[BO_4]^{5-}$ ions isolates the Eu^{2+} ions from one another, *i.e.*, it acts as a shield of the Eu^{2+}-Eu^{2+} non-radiative energy transfer processes, and is one of the reasons for the strong Eu^{2+} luminescence in the borate host matrices [37]. Moreover, the high emission energy in the UV range makes non-radiative quenching highly improbable in favor of a high radiative transition probability. Besides, the band gap in a very ionic compound like SrB_4O_7 is expectedly high, which also minimizes the probability for thermally assisted delocalization of the excited 5d electron into the conduction band.

4.1.2. Elastic properties

The elastic properties of SrB_4O_7 were analyzed at ambient pressure based on *ab initio* calculations in order to evaluate its potential as a host compound of luminescent ions for high-pressure applications. SrB_4O_7 crystallizes in an orthorhombic crystal system, which gives rise to 9 independent elastic constants [55]. As presented in **Table S2** in SI, the calculated values of the elastic constants are in better agreement with the experimental values than the calculations based on the non-empirical ionic-crystal model [56,57]. The bulk modulus (B), shear modulus (G), Young modulus (E) and Poisson's ratio (ν), which describe the main elastic properties of a material, can be obtained by analytical expressions from the reference [58] in the Voigt and Reuss approximations assuming uniform stress or strain throughout a polycrystalline compound [59,60]. Hill indicated that the Voigt and Reuss approximations have limitations and pointed out that the actual elastic moduli can be estimated by the arithmetic mean of the two bounds [61]. The elastic moduli of the orthorhombic SrB_4O_7 at 0 GPa are compiled in **Table S3** in SI. The value of the Hill bulk modulus, $B_H = 149.33$ GPa, agrees well with the value obtained from the theoretical data with the Birch-Murnaghan equation of state [62], *i.e.*, $B_0 = 150.17$ GPa. This fact indicates a high reliability of the calculated elastic constant values and the consistency of calculations.

The bulk modulus ($B = 149.33$ GPa) can be considered as a measure of the resistance to volume changes and the shear modulus ($G = 123.22$ GPa) - as a measure of resistance to reversible deformations upon shear stress. Therefore, this material is more resistant to compression than to shear stress. The B/G ratio introduced by Pugh describes the relationship between the plastic properties and the elastic moduli of materials [63]. If $B/G > 1.75$, the material exhibits ductility. Otherwise, the material is classified as brittle. At 0 GPa, the B/G ratio of SrB_4O_7 is around 1.2 and would thus, be classified as brittle at ambient conditions. Poisson ratio provides

information about the characteristics of the bonding forces, and the value of $\nu = 0.25$ is considered as the lower limit of the central forces in the solid [62]. The investigated compound has a Poisson ratio of $\nu = 0.176$ that agrees with the previously described brittle nature of the solid. It indicates a low degree of elasticity of crystalline SrB_4O_7, which is a consequence of the very strong ionic bonds and highly condensed network of $[BO_4]^{5-}$ tetrahedra within the crystal structure. The elastic anisotropy is one of the most important elastic properties of materials for both engineering and crystal physics, since it is related to the possibility of inducing micro-cracks in materials [64]. This property is quantified by the universal elastic anisotropy index A_U. The more this index differs from 0, the more elastically anisotropic the structure is [65]. The A_U at 0 GPa is 0.071, further indicating that SrB_4O_7 is slightly anisotropic, in agreement to the orthorhombic crystal system it crystallizes in at ambient pressure.

To conclude this section, the average sound wave velocity ($\nu_m = 6110.63$ m s^{-1}) within the Debye approximation was calculated. From the shear modulus G and the bulk modulus B, longitudinal ($\nu_l = 8851.89$ m s^{-1}) and transverse ($\nu_t = 5548.85$ m s^{-1}) elastic wave velocities can be obtained [66]. The Debye temperature (θ_D), a fundamental parameter that correlates with the mechanical and thermodynamic properties of a solid such as specific heat capacity and melting temperature, can be estimated from the average wave velocity [67]. For SrB_4O_7, we find a value of $\theta_D = 895.11$ K, which is perfectly well related to the previously indicated rigid structure with the highly condensed $[BO_4]$-based network. A high Debye temperature is a usually beneficial material property [68] for a host compound for luminescent ions, as is e.g., demonstrated by the thermally stable red-emitting phosphors $Sr[LiAl_3N_4]$:Eu^{2+} (SLA:Eu^{2+}) [20] and $Sr[Li_2Al_2O_2N_2]$:Eu^{2+} (SALON:Eu^{2+}) [19].

4.1.3. Vibrational properties

The unit cell of SrB_4O_7 gives rise to 72 normal vibrational modes in the center of the Brillouin zone (19 A_1 + 17 A_2 + 17 B_1 + 19 B_2), which are all Raman-active. Since A_1, B_1, and B_2 are polar modes, they are also IR-active and can exhibit a transversal optical – longitudinal optical (TO-LO) splitting of vibrational modes in the Raman and IR spectra. Therefore, 69 TO modes and 52 LO modes could potentially appear in the Raman spectrum. Fig. 1**b** depicts the Raman spectrum at RT measured in backscattering geometry, and it mainly contains lines due to the A_1 and A_2 modes by means of the Raman selection rules. It exhibits 13 Raman-active modes in the lower-energy range, from 200 to 700 cm^{-1}, *i.e.*, the modes at around 263, 283, 325, 364, 417, 431, 445, 491, 514, 536, 557, 580 and 635 cm^{-1}. These modes agree well with
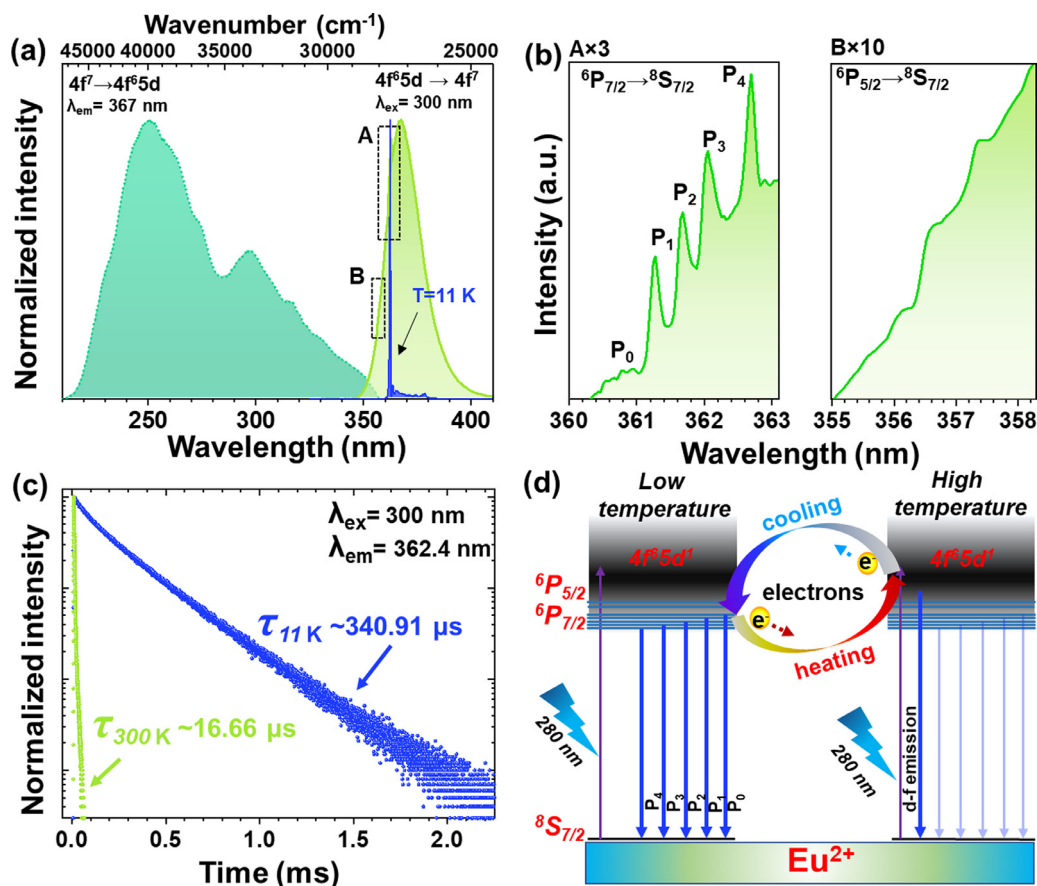
Fig. 2. a) Photoluminescence excitation (dark green area) and emission (light green area) spectra of Eu^{2+} in the SrB_4O_7 matrix at ambient conditions. For comparison, the emission spectrum (blue) measured at 11 K is also included. b) The magnified fine structure of the emission bands (at RT) attributed to the $4f^7 \rightarrow 4f^7$ transitions of Eu^{2+}, *i.e.*, $^6P_{7/2} \rightarrow {}^8S_{7/2}$ (left) and $^6P_{5/2} \rightarrow {}^8S_{7/2}$ (right). c) Luminescence decay curves measured at 11 K and 300 K, at $\lambda_{ex} = 300$ nm, $\lambda_{em} = 362.4$ nm. d) A simplified diagram of the energy levels for Eu^{2+} in the SrB_4O_7 matrix, at low- and high-temperature conditions.

the A_1 and A_2 modes reported in ref. [69], except for the mode at 445 cm^{-1} that could be assigned to a B_1 mode. In fact, most of the Raman modes of high (low) intensity can be ascribed to modes transforming like A_1 (A_2) [57,69], with A_2 modes only allowed for backscattering configuration with crossed polarization. However, taking into account our theoretical calculations, the modes at 445, 514 and 557 cm^{-1} may be correspondent to B_1, B_1, and B_2 modes, respectively (see **Table S4**). In isostructural PbB_4O_7, three similar modes have been associated with the bending mode (ν_4) of free tetrahedral $[BO_4]$ units, the stretching mode (ν_s) of metaborate ring groups, and the stretching mode (ν_1) of the $[BO_4]$ units [70]. In addition, Raman spectra in the 1100-1750 cm^{-1} range consist of 5 broad bands centered at 1172, 1282, 1346, 1498, and 1651 cm^{-1}, respectively. Only the first one is close to the A_2 mode reported at 1167 cm^{-1} in ref. [69], and this is attributed to the B-O stretching vibration [71].

Fig. S3 in SI shows the calculated total one-phonon density of states (1-PDOS) and the partial 1-PDOS for each atom. It can be observed that low-frequency modes below 200 cm^{-1} are dominated by the movement of Sr atoms. Mid-frequency modes, between 200 and 800 cm^{-1}, are dominated by the vibration of O atoms with some contribution of B atoms above 500 cm^{-1}. Finally, the high-frequency modes above 800 cm^{-1} are dominated by vibrations of B atoms, with some contribution of O atoms. The vibrational modes of AMO_4 compounds were discussed in terms of internal and external modes of rigid $[MO_n]$ polyhedra [72,73]. Similarly, $A_xB_4O_7$ borates could be discussed in terms of internal and external modes of $[B_2O_7]$ units or in terms of the internal and ex-

ternal modes of $[BO_4]$ units, since $[BO_4]$ polyhedra constitute the rigid units of these compounds [74–76].

4.1.4. Photoluminescence Properties

The optically active Eu^{2+} ion is isoelectronic to Gd^{3+} and has an $^8S_{7/2}$ ground level arising from the $4f^7$ configuration. The main difference between them is the lower charge of the Eu^{2+}, which makes it more covalent and, hence, leads to a smaller energy gap between the first excited $4f^65d^1$ and the $^8S_{7/2}$ ground level than for the Gd^{3+} ion. The energy level diagram of the Eu^{2+} is quite simple, *i.e.*, the $^8S_{7/2}$ ground level with a large energy gap of around 27000 cm^{-1} to the lowest excited level, and the ^6P_J, ^6I_J, and ^6D_J excited multiplets of the $4f^7$ ground configuration. The $4f^7 \rightarrow 4f^7$ emissions are characterized by typical decay times ranging from hundreds of microseconds to several milliseconds [77,78]. The $4f^65d^1$ levels, often obscuring the excited levels of the $4f$ configuration (because the lowest energy of the $4f^65d$ configuration in Eu^{2+} is usually lower than the energy of the ^6P_J levels), give rise to $4f^65d^1 \rightarrow 4f^7(^8S_{7/2})$ emission, which shows much faster decay times in the order of 1 μs. A detailed discussion of the Eu^{2+} energy level diagram can be found in ref. [79].

The Eu^{2+} excitation spectra at RT typically consist of broad bands associated to parity-allowed, inter-configurational electronic transitions between the $^8S_{7/2}$ ground level of the $4f^7$ configuration and the multiplets of the $4f^65d^1$ excited configuration [80,81]. In the emission spectrum recorded at RT, a single broad band corresponding to the $4f^65d^1 \rightarrow 4f^7(^8S_{7/2})$ transition is observed (see

Fig. 2**a**) [21]. While energies of the $4f^7$ levels are hardly influenced by the matrix, as these electrons are shielded by the 5s and 5p electrons, the energies of the $4f^65d^1$ levels are highly sensitive to the magnitude of the crystal-field interaction experienced by the Eu^{2+} ions in the host lattice and the degree of bond covalency [82]. Thus, the emission energy associated with the parity-allowed $4f^65d^1 \rightarrow 4f^7(^8S_{7/2})$ transitions may vary, for example, from 367 nm in SrB_4O_7 [37,38] to e.g., 733 nm in CaO [83].

The excitation spectrum of Eu^{2+} ions in SrB_4O_7 tetraborate is presented in Fig. 2**a**. In the excitation spectrum, two components can be distinguished as two intense, broad bands in the UV range, starting from about 210 nm ($\sim$ 47619 cm^{-1}) to 355 nm ($\sim$ 28169 cm^{-1}) and peaked at around 251 and 297 nm [37,38,84], in agreement to the pioneering findings by Meijerink *et al.*[38]. Given the low approximate C_{4v} site symmetry at the Sr sites in SrB_4O_7, which leads to a splitting of the 5d orbitals into four components (transforming like $a_1(z^2) + b_1(x^2-y^2) + b_2(xy) + e(xz, yz)$), which additionally couple to the six 4f electrons in the excited configuration, the excited energy level landscape of Eu^{2+} in this compound is very dense and does not readily allow unambiguous assignments of the excitation bands.

Concerning the luminescence, if the lowest states of the excited $4f^65d^1$ configuration are at the higher energies than the excited $4f^7$ multiplets, narrow intra-configurational $4f^7 \rightarrow 4f^7$ emission lines from the $^6P_{7/2}$ [30,85–92], $^6P_{5/2}$ [30,88,93] and $^6I_{7/2}$ [94] multiplets to the $^8S_{7/2}$ ground state can be observed. According to Blasse [87], such a situation can be easily found in host matrices with hard anions giving rise to ionic Eu-ligand bonds, such as fluorides. However, other conditions must also be fulfilled, *i.e.*, a small crystal-field splitting of the 5d orbitals of Eu^{2+}, and a small Stokes shift of the broad band emission, associated with the slight difference between the equilibrium positions of the $^8S_{7/2}$ ground state and the lowest $4f^65d$ state in the configuration coordinate model. In addition, Ryan *et al.* also considered the existence of a small exchange interaction between the six 4f electrons and the 5d one of the excited configurations as another condition to be taken into account [79]. As already mentioned, these conditions usually occur in fluoride matrices [95], but some oxide hosts, such as $SrBe_2Si_2O_7$, $BaBe_2Si_2O_7$, SrB_4O_7, and $SrAl_{12}O_{19}$ [38,96,97], also show these characteristics. In the case of SrB_4O_7, it is worth noting that the formally trivalent B^{3+} ions located in the neighborhood of the Eu^{2+} ions, are small ions with a high charge density and, thus, additionally withdraw electron density from the O^{2-} ligands. Due to the high B:Sr ratio in SrB_4O_7, the Eu-O bond has an overall high ionic character, which is connected to a small exchange interaction between 4f and 5d electrons [38]. Moreover, the rigid network in the crystal structure (also leading to the high Debye temperature) renders the Stokes shift of the $4f^65d^1 \rightarrow 4f^7(^8S_{7/2})$-related emission small [87,98].

It is essential to mention that although these calculations give values for the crystal-field strength and the splitting of the multiplets are more significant than those found in fluoride host matrices, they are still lower than those typically found in oxide hosts. Thus, the Eu^{2+} ions replace the Sr^{2+} ones located in the large cavities formed by the interconnected $[BO_4]$ tetrahedra, and the crystal-field interaction by the lanthanide ion is weak given the large coordination number of 9. This results in low splitting of the multiplets of the $4f^7$ ground and the $4f^65d$ excited configurations. In addition, the highly condensed borate network in SrB_4O_7 and the electron-withdrawing nature of the various B^{3+} ions make the oxygen ligands chemically hard and lead to a rather ionic Eu-O bond. With decreasing Sr/B ratio such as in $Sr_3(BO_3)_2$:Eu^{2+} (emission at 590 nm) or the extreme case of SrO:Eu^{2+} (emission at 625 nm), the $4f^65d^1 \rightarrow 4f^7$ transition of Eu^{2+} systematically shifts to lower energies in agreement with the expectation of a more cova-

lent Eu-O bond. Meijerink *et al.* found in Eu^{2+}-doped SrB_4O_7 that the lowest state of the 4f^{6}5d first excited configuration is only $\sim$ 130 cm^{-1} above the lowest Stark state of the $^6P_{7/2}$ level [38]. This low value offers the possibility to investigate a stimuli-induced configuration crossover.

The photoluminescence spectrum in the UV region from $\sim$ 345 to $\sim$ 410 nm upon the excitation at 300 nm is depicted in Fig. 2**a, b** and supports the above argument. At 11 K, it consists of a single sharp line at 362.4 nm (Fig. 2**a**; blue area), at a similar wavelength reported by Meijerink *et al.*, [38] and can be assigned to the $4f^7 \rightarrow 4f^7$ intra-configurational transitions between the two lowest Stark levels of the $^6P_{7/2}$ and $^8S_{7/2}$ multiplets of the Eu^{2+} ions. In addition, this peak is accompanied by vibronic sidebands on the low energy (long wavelength) side (see **Fig. S4** in SI). These bands simultaneously involve the emission of the $^6P_{7/2} \rightarrow {}^8S_{7/2}$ electronic transition of the Eu^{2+} ion and vibronic replicas based on coupling to vibrational modes of the host [99]. The luminescence decay curve depicted in Fig. 2**c** additionally proves the expected forbidden nature of this sharp line for a $4f^7 \rightarrow 4f^7$ transition based on the large effective lifetime ($\tau_{eff} = \int t \cdot I \, dt / \int I dt$), of $\tau_{11\,K} \approx 340.9$ μs compared to the otherwise shorter decay time of the $4f^65d^1 \rightarrow 4f^7(^8S_{7/2})$ broad-band emission of $\tau_{300\,K} \approx 16.66$ μs.

In order to better understand the mechanism of the Eu^{2+} emission at RT, the normalized emission spectra with increasing temperature values from 11 K to 200 K were acquired and are shown in **Fig. S5a** in SI. The Eu^{2+} emission spectrum changes strongly with temperature. Just above 20 K, one can observe not only a sharp peak at 362.4 nm, but also new sharp features at higher energies (shorter wavelengths) together with the underlying broadband peak at $\sim$ 367 nm, due to the thermally induced population of the upper $^6P_{7/2}$ Stark states and the lowest levels of the $4f^65d$ excited configuration, respectively, as shown in the simplified energy level diagram in Fig. 2**d**. The relative intensity of this broad band dramatically increases with temperature, not only masking the vibronic sidebands but also partially the other sharp peaks ($4f^7 \rightarrow 4f^7$ emission lines). That is why the emission spectrum at RT is the result of a convolution of Eu^{2+}-related radiative transitions of different nature, *i.e.*, the intense $4f^65d^1 \rightarrow 4f^7(^8S_{7/2})$ inter-configurational, broad-band emission, with a maximum at around 367 nm ($\sim$ 27248 cm^{-1}), and a group of five superimposed narrow and weak $4f^7(^6P_{7/2}) \rightarrow 4f^7(^8S_{7/2})$ intra-configurational emission lines in the range from 360 to 363 nm. In addition, there are emission peaks observed at around 357 nm, which are plausibly related to the $4f^7(^6P_{5/2}) \rightarrow 4f^7(^8S_{7/2})$ transition. The difference in energy between the vibronic bands and the sharp line corresponds to the energy of one phonon and range from 200 to 1200 cm^{-1}, *i.e.* they cover almost all vibrational modes analyzed in this matrix [38]. Fig. 2**b** presents the magnified A and B area marked in Fig. 2**a**, and shows the detailed structure of this emission represented by five sharp lines. They center at 360.9 nm ($\sim$ 27708 cm^{-1}), 361.4 ($\sim$ 27670 cm^{-1}), 361.8 ($\sim$ 27639 cm^{-1}), 362.1 ($\sim$ 27616 cm^{-1}) and 362.7 nm ($\sim$ 27571 cm^{-1}), labelled as P_0 to P_4, respectively. The P_0 peak corresponds to the zero-phonon line of the broad band $4f^65d^1 \rightarrow 4f^7(^8S_{7/2})$ inter-configurational emission, whereas P_1 to P_4 are associated with the transitions from the four crystal-field (Stark) sublevels of the $^6P_{7/2}$ multiplet to the $^8S_{7/2}$ ground level. The total splitting is in the order of $\sim$100 cm^{-1}. The $^8S_{7/2}$ level only shows negligible crystal field splitting (< 1 cm^{-1}) based on its single orbital degeneracy ($2L + 1 = 1$) and the solely intermediate degree of spin-orbit coupling that makes L still a well-defined quantum number [100]. Meijerink *et al.* have presented a schematic configurational coordinate diagram for Eu^{2+} in SrB_4O_7, justifying the presence of emission peaks at low temperature and showing the energy difference between the high-
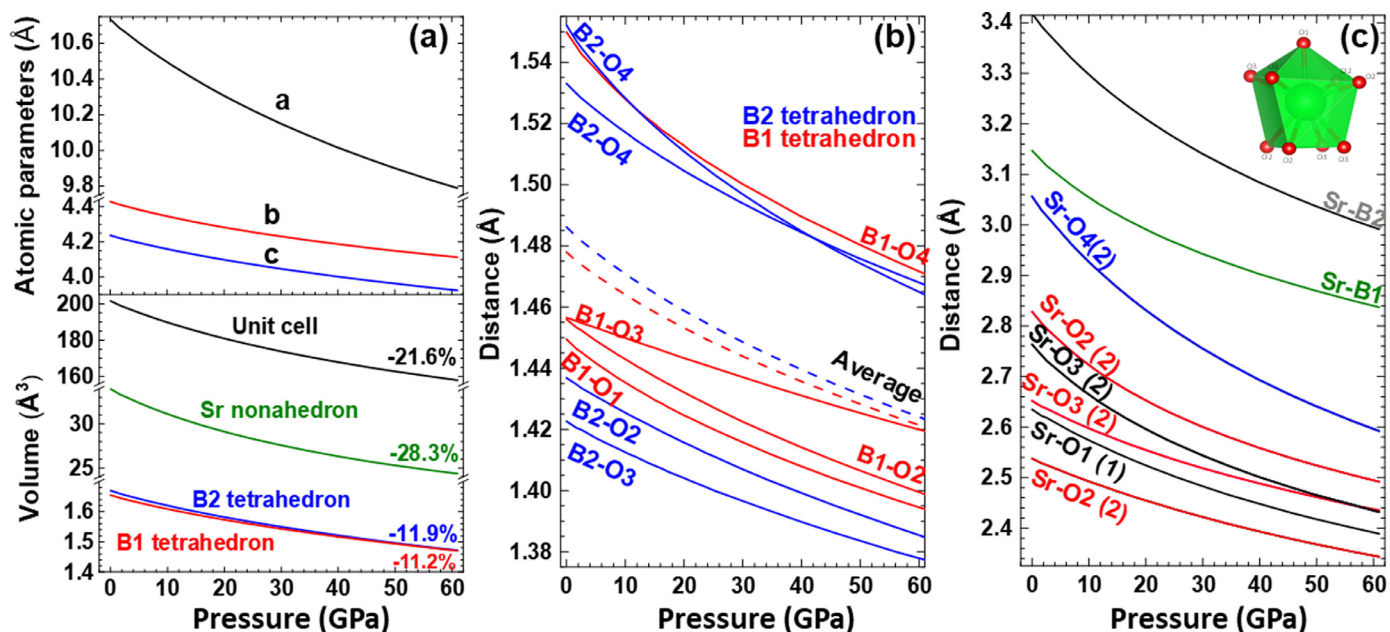
Fig. 3. Pressure dependence of a) cell parameters (top); unit cell volume, [SrO$_9$] polyhedron and [BO$_4$] tetrahedra (bottom) of SrB$_4$O$_7$ based on *ab initio* calculations. b, c) Evolution of atomic bonds in the polyhedral units based on *ab initio* calculations. The [SrO$_9$] coordination unit is displayed as an inset at the top of c).

est $^6P_{7/2}$ Stark level and the ground state of the 4f^{6}5d configuration of 130 cm^{-1} [38]. They also determined a Stokes shift of 750 cm^{-1} for the 4f^{6}5d^1 → 4f^7 transition. Another interpretation could be that the P$_{0-4}$ lines are related to the one-phonon repetition of the zero-phonon line [90,92]. However, the theoretical calculations of the lowest phonon energies showed only six Raman and IR active phonon modes ranging from 95 to 150 cm^{-1} (see **Table S5**), which do not match well the (P$_1$-P$_0$=) 38 cm^{-1}, (P$_2$-P$_0$=) 69 cm^{-1}, (P$_3$-P$_0$=) 92 cm^{-1}, and (P$_4$-P$_0$=) 137 cm^{-1} energy differences found in the emission spectrum. Hence, this assignment is doubtful.

As a conclusion, SrB$_4$O$_7$ tetraborate fulfills all the requirements formulated by Blasse to allow emitting both inter- and intra-configurational electronic transitions [87]. At low temperature and under direct excitation, the 4f^7($^6P_{7/2}$)→4f^7($^8S_{7/2}$) emission peaks are dominant, while a broad-band emission due to the 4f^{6}5d^1 → 4f^7 transition is observed at higher temperatures [38]. Furthermore, no emission from Eu^{3+} ions above 580 nm was observed, but features related to the additionally present Sm^{2+} ions appeared above ∼ 685 nm, which were already presented and discussed in our previous work [39].

4.2. Properties at high pressure

4.2.1. Structural and elastic properties

In order to definitively clarify the impact of high pressure on the crystal structure, mechanical and vibrational properties of orthorhombic SrB$_4$O$_7$, we have carried out *ab initio* calculations. In this system, the strontium atoms are positioned in the nine-fold coordinated polyhedron in a rigid three-dimensional [B$_4$O$_7$] network of vertex-sharing [BO$_4$] tetrahedra. The *ab initio* atomic coordinates and cell parameters at 61 GPa pressure are compared to the values at zero pressure in **Table S1**. The evolution of the unit cell parameters and volume as a function of pressure in the *Pmn2$_1$* structure of SrB$_4$O$_7$ is displayed in Fig. 3**a (top)**. All the cell parameters decrease with increasing pressure from 0 to 60 GPa, although the *a* axis is more compressible than the other two axes, indicating that compression of the structure is anisotropic under hydrostatic pressure. The linear axial compressibility (K_i) of the crystal axis can

be calculated using the following equations:

$$K_a = \frac{-1}{a_0}\frac{\mathrm{d}a}{\mathrm{d}p}; \; K_b = \frac{-1}{b_0}\frac{\mathrm{d}b}{\mathrm{d}p}; \; K_c = \frac{-1}{c_0}\frac{\mathrm{d}c}{\mathrm{d}p} \qquad (1)$$

Using equations (1), we obtained K_a=2.15·10^{-3} GPa, K_b =1.77·10^{-3} GPa and K_c=1.75·10^{-3} GPa. The evolution of the unit cell volume and the polyhedral units under pressure is shown in Fig. 3a **(bottom)**. It was found that there is a decreasing tendency and no volume discontinuity during compression. The compression of the unit cell is dominated by the softer polyhedral unit, in this case, the strontium nonahedron, which decreases its volume by ∼ 28.3% in the studied pressure range. This is a consequence of the continuous decrease of the bond lengths (B-O, Sr-O, and Sr-B) upon compression (see Fig. 3b and c).

In addition, we investigated the evolution of the electronic bandgap under pressure by DFT calculations. The *ab initio* calculated electronic band structures along the high symmetry directions in the first Brillouin zone at 0 GPa and 54 GPa are displayed in Fig. 4**a and** 4**b**, respectively. The band structures show a typical semiconductor-like distribution. The bands are very flat with little dispersion, which agrees with the very ionic nature of the chemical bonds in SrB$_4$O$_7$ that lead to highly localized and polarized states in real space and consequently, no covalent and extended bond formation within the periodic structure of the crystal. The edge of the conduction band (CB) changes with pressure, while the one of the valence band (VB) negligibly alters at the Γ point within the whole pressure range studied.

At zero pressure, the VB maximum is located at the R point, giving rise to a wide indirect band gap (R-Γ) of 7.16 eV. With increasing pressure, this gap increases linearly until approximately 9 GPa (see Fig. 4**c**). The maximum value of band gap, 7.49 eV, is achieved at 26.2 GPa where the maximum VB is shifted to the U point, and, then, it slowly decreases with increasing pressure. Interestingly, the band structure becomes even less dispersive in reciprocal space at high pressures, which formally implies an even more ionic nature of the chemical bonds in the compound and perfectly agrees with the generally increasing band gap.
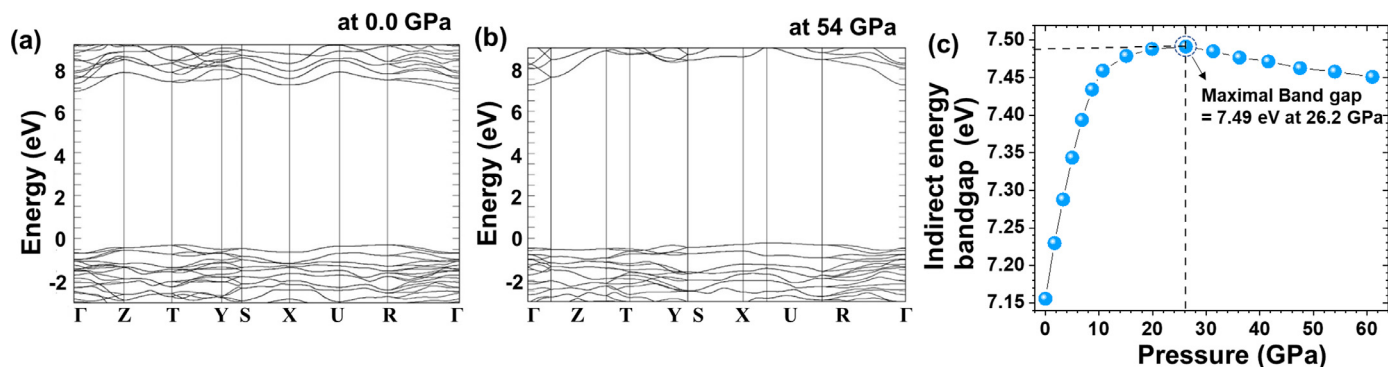
Fig. 4. Electronic band structure of SrB_4O_7 at a) 0 GPa and b) 54 GPa. c) Pressure evolutions of the electronic bandgap

For the sake of completeness, we also analyzed the elastic properties of SrB_4O_7 under pressure. When a non-zero uniform stress is applied to a crystal, the relevant magnitudes describing its elastic properties are no longer the elastic constants (C_{ij}). Instead, the elastic stiffness coefficients (B_{ij}) should be used [101]. In the special case of the hydrostatic pressure, P, applied to the orthorhombic crystal, the elastic stiffness coefficients are related to the elastic constants by the following expressions [101,102]:

$$B_{ii} = C_{ii} - P \quad \text{for } i = 1 \text{ to } 6 \tag{2}$$

$$B_{ij} = C_{ij} + P \quad \text{for } i \neq j \text{ and } i, j = 1 \text{ to } 3 \tag{3}$$

$$B_{ij} = C_{ij} \quad \text{for } i \neq j \text{ and } i, j = 4 \text{ to } 6 \tag{4}$$

with C_{ii} being the elastic constants evaluated at the current stressed state. It should be noted that for zero applied pressure, the B_{ij} values are reduced to the conventional constants C_{ij}.

Fig. 5a shows the pressure dependence of the elastic stiffness coefficients, B_{ij}. They increase rapidly with pressure, except of B_{55}, B_{66}, and B_{44}. The coefficients B_{55}, and B_{66} have similar values, while B_{44} remains almost constant in the whole pressure range studied. If the crystal is mechanically stable at zero pressure, the Born stability criteria involving the elastic constants are fulfilled [103]. However, if the crystal is subjected to hydrostatic pressure, the previous criteria should be modified by means of the elastic stiffness coefficients, which leads to a modification of the Born stability criteria. A crystal at elevated pressures is considered mechanically stable if the representation matrix of the elastic stiffness tensor, (B_{ij}), is positive-definite [104]. Our study shows that all the eigenvalues of the matrices B_{ij} are positive; therefore the orthorhombic SrB_4O_7 is mechanically stable up to the maximum pressure (61 GPa) regarded in the present study.

The elastic stiffness constants allow to obtain the elastic properties of the material at any hydrostatic pressure. All the relationships of the theory of elasticity employed at zero pressure can be applied to a crystal subjected to high-pressure compression using the elastic stiffness coefficients B_{ij} [105,106]. The pressure dependences of the B, G, E elastic moduli, Poisson's ratio ν, and the B/G ratio for SrB_4O_7 are shown in Fig. 5b-d. The bulk modulus (B) increases rapidly with pressure, while the shear modulus increases only slightly. The B/G ratios are all over 1 from 0 to 61 GPa, which indicates that strontium tetraborate is more resistant to volume compression than to shear deformation. Moreover, the B/G ratio increases rapidly with pressure. At 30 GPa, it is $B/G = 1.77$, and, therefore, the material becomes ductile. Poisson's ratio (ν) corroborates this behavior change. Around 24 GPa, it is $\nu = 0.25$, which appears reasonable since successively higher pressures enforce smaller distances between the different ions, which

is partially released by a successive release of strain in the directions orthogonal to the direction of compression. A higher Poisson ratio at elevated pressures indicates that a compound becomes more elastic then, which agrees with the findings on the elastic moduli.

4.2.2. Vibrational properties

We have carried out HP Raman scattering experiments up to $\sim$ 17 GPa, and the Raman spectra at selected pressures are shown in **Fig. S6a**. The signal/noise ratio decreases as the pressure increases, which is a commonly encountered phenomenon. We were able to trace the experimental pressure dependence of the six most intense Raman-active modes of A_1 symmetry during the compression and decompression processes (see Figs. 6, **S6b and S7** in SI). The six observed Raman-active modes of SrB_4O_7 shift monotonously, suggesting no phase transition as the pressure increases up to 16.6 GPa. This agrees with the emission spectra and other reports on SrB_4O_7 under pressure [107,108]. Due to the bond shortening caused by the compression, all the observed Raman peaks show a shift towards the high wavenumbers. As shown in the pressure dependences of the experimental (symbols) and theoretical (lines) Raman-active mode frequencies (see Fig. 6), the experimental data agrees with theoretical calculations up to 16 GPa, *i.e.*, show that all Raman modes have a positive frequency-pressure coefficient (see **Table S5**). As shown in **Fig. S7**, the evolution of the theoretical Raman-active mode frequencies in SrB_4O_7 shows a sublinear pressure dependence up to 25 GPa, which is also confirmed by our experiments up to 16 GPa. However, for the sake of simplicity, in **Table S5** we have included the theoretical zero-pressure linear coefficients obtained from fits to 5 GPa. Similarly, the zero-pressure linear coefficients of the experimental modes centered at 283, 364, 431, 491, 580 and 635 cm^{-1} are 2.8, 2.2, 2.3, 2.3, 1.9 and 2.6 cm^{-1}/GPa, respectively. These pressure coefficients are in good agreement with those of the theoretical A_1^3, A_1^5, A_1^6, A_1^7, A_1^8 and A_1^9 modes (see **Table S5**). It is observed that the modes with smaller pressure coefficients are those with wavenumbers below 640 cm^{-1}, and the modes with the largest pressure coefficients are those with wavenumbers above 740 cm^{-1}.

4.2.3. Photoluminescence properties and pressure sensing performance

The appearance of the emission spectrum of Eu^{2+} in SrB_4O_7 based on dominant emission from the excited $4f^65d^1$ or $4f^7$ configurations depends on different stimuli. As for other divalent lanthanide ions, the most important ones are: I) a temperature-induced excitation from the excited emitting $4f^7$ states to the lowest states of the $4f^65d$ configuration, which may lead to enhancement of the $4f^65d^1 \rightarrow 4f^7$ emission at the expense of the $4f^7 \rightarrow 4f^7$ luminescence, as already observed for the luminescence
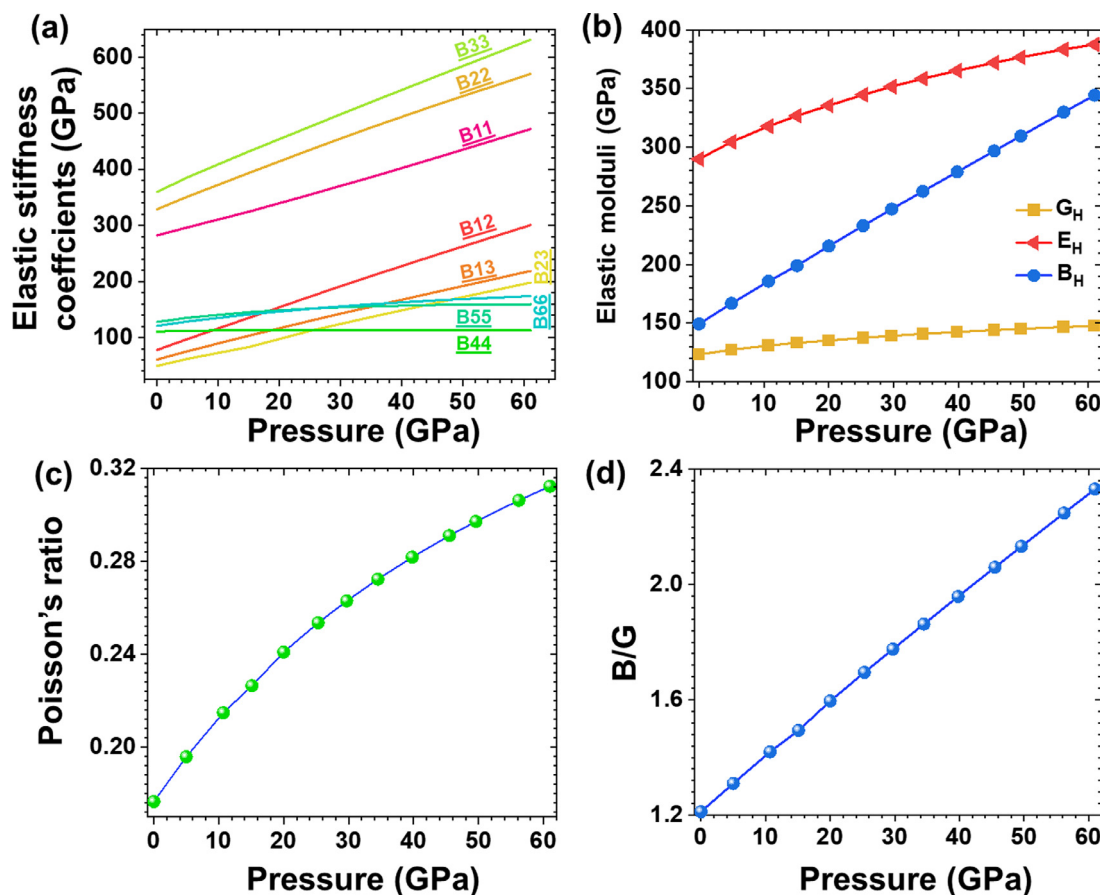
Fig. 5. a) elastic stiffness coefficients (B_{ij}) in SrB_4O_7. b-d) Pressure dependences of *B, E, G* (b), ν (c), and *B/G* (d) parameters in SrB_4O_7 according to *ab initio* calculations.

in SrB_4O_7:Eu^{2+} above 11 K (see **Fig. S5a, b** in SI) [101]; and II) a pressure-induced tuning of the energy separation between configurations and their respective levels.[109,110] Thus, pressure can increase the mixing of $4f^6 5d$ to $4f^7$ wave functions, with clear impact on the emission probabilities and intensities. However, the specific response of the electronic state to pressure, *i.e.*, the changes in its energy and the probability of absorption, emission, or non-radiative relaxation, depends on the extension of the involved orbitals in the excited states and thus, also the magnitudes of the crystal-field and covalency effects [110].

By focusing on the optical properties of Eu^{2+}, as the pressure increases, the different polyhedral volumes of the matrix decrease, especially the $[EuO_9]$ and $[SrO_9]$ polyhedra that show the largest compression rate, *i.e.*, 28.3 % at 60 GPa with respect to the volume at ambient pressure, as already mentioned. Consequently, the interactions between the seven *f*-electrons, *i.e.*, the free-ion interactions, are affected by the valence electrons of the nine oxygen ligands. In general, the major free-ion interactions, *i.e.*, the Coulomb interelectronic repulsion and the spin-orbit coupling decrease with pressure due to a generally increasing covalency, while the magnitude of the crystal-field interaction increases, albeit with a lower rate. Typical consequences are the decrease of the transition energy (red-shift), due to the overall contraction of the configurations, and the simultaneous increase of the splitting of the multiplets. However, different rates of change are expected for the multiplets of the excited and ground configurations. This is because the variations in the energies of the 4f multiplets are relatively small [109,111], on the order of a few cm^{-1}/GPa, whereas they can be very large for the multiplets of the excited configuration involving *5d* states. These may range from tens to hundreds of cm^{-1}/GPa, as shown in **Table S6** in SI.

In order to investigate the effect of lattice compression on the UV emissions of Eu^{2+} ions in the synthesized micron-sized SrB_4O_7 material, high-pressure photoluminescence experiments were conducted in a diamond anvil cell (DAC) up to $\sim$ 58 GPa at RT. The schematic configuration of the applied DAC and a simplified scheme of the experimental setup used for high-pressure luminescence measurements are presented in Fig. 7**a**. The pressure-induced variations of the relative luminescence intensities of the inter- and intra-configurational transitions of Eu^{2+}, upon the 280 nm light excitation are shown in Fig. 7**b**. The use of 280 nm excitation light (close to the optimal excitation wavelength) is due to the availability of a high-power, focusable light source. The intensity of the broad emission band $4f^6 5d^1 \rightarrow 4f^7(^8S_{7/2})$ gradually decreases up to $\sim$ 35 GPa, above which the band is no longer clearly observed as its intensity is close to the noise level. Inversely, the $4f^7(^6P_{7/2}) \rightarrow 4f^7(^8S_{7/2})$ intra-configurational emission starts to increase in intensity, almost abruptly, above $\sim$ 20 GPa and become the only emissions above $\sim$ 30 GPa, together with broad vibronic bands, already observed in the normalized emission spectra at low temperature in **Fig. S5a, b** in the SI. The emission intensities of the $4f^7(^6P_{7/2}) \rightarrow 4f^7(^8S_{7/2})$ peaks (P_4 peak) were estimated by Gaussian deconvolution (Gaussian fitting) using the integrated peak area of the Gauss bands with abscissa of wavelength (in nm) as a measure for that. Over the entire measured high-pressure range, the intensity enhancement of the $4f^7(^6P_{7/2}) \rightarrow 4f^7(^8S_{7/2})$ peak is estimated to be about three orders of magnitude ($\sim$800 times), as depicted in Fig. 7**d** and the histogram in the inset of Fig. 7**d**. In addition, as shown in **Fig. S8** in SI, the Eu^{2+} emission band changes back to its initial shape, and the $4f^7 \rightarrow 4f^7$ emission intensity also returns to its initial intensity upon compression, confirming that the tendency in the intensity change of both $4f^7 \rightarrow 4f^7$ and $4f^6 5d^1 \rightarrow 4f^7$
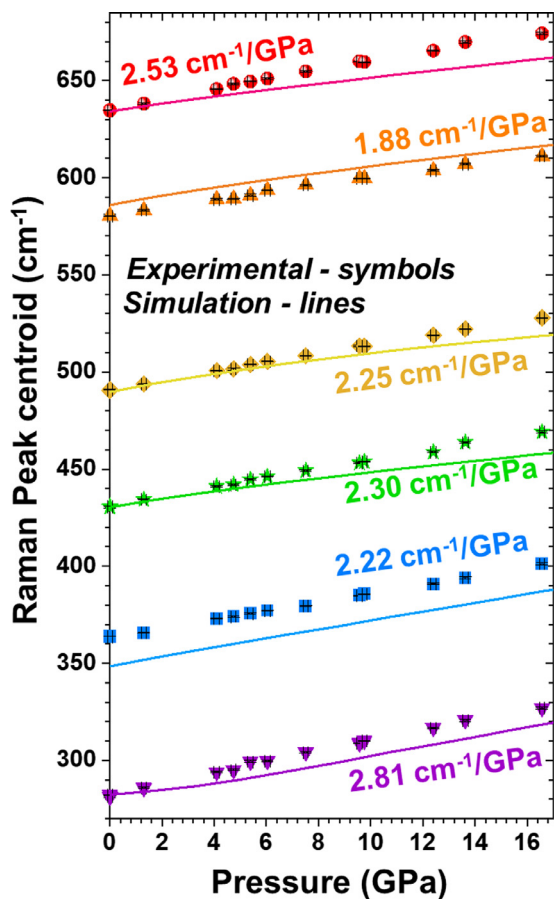
Fig. 6. Pressure dependences of the experimental (symbols) and theoretical (solid lines) Raman-active mode wavenumbers.

emissions of Eu^{2+} in the sample is reversible in compression and decompression cycles.

The $4f^7 \rightarrow 4f^7$ emission peaks also show a fully reversible red-shift under pressure (see Fig. 7c), due to the overall contraction of the $4f^7$ ground configuration, which results in a reduction of the energetic separation between the ground state and the excited $^{2S+1}L_J$ multiplets, as shown in the simplified energy level diagram in Fig. 7e. The peak centroid of the Eu^{2+} transition $^6P_{7/2} \rightarrow {}^8S_{7/2}$ (P_4) reversibly shifts from 362.1 nm at ambient conditions to ~372.4 nm at 58.7 GPa, with a rate of -12.84 cm^{-1}/GPa (or 0.17 nm/GPa), being comparable to the pressure sensitivity of the wavelength of the $^5D_0 \rightarrow {}^7F_0$ transition of Sm^{2+} in this matrix [39]. It is of great importance that the position of the peak centroid of the $^6P_{7/2} \rightarrow {}^8S_{7/2}$ transition as a function of temperature (see **Fig. S5c**) shows an extremely weak temperature dependence, i.e., $|d\lambda/dT| = 4.8 \times 10^{-4}$ nm K^{-1} ($\sim$ -0.037 cm^{-1}/K). The combination of the huge pressure-induced intensity enhancement accompanied by the significant red-shift of the Eu^{2+} $4f^7 \rightarrow 4f^7$ emission lines, and negligible temperature dependence of the corresponding $^6P_{7/2} \rightarrow {}^8S_{7/2}$ transition peak centroid, make the Eu^{2+}-doped SrB_4O_7 material an excellent pressure gauge for high pressures.

In order to examine the validity/reliability of the discussed signal enhancement and explore the influence of different Eu^{2+} contents on the enhancement and red-shift of the P_4 peak, a series of high-pressure photoluminescence experiments were performed using SrB_4O_7 with a higher Eu^{2+} content, i.e. 0.09 Eu^{2+} (9 mol.%). As expected, the normalized emission spectra recorded in the pressure range from ~ 1.3 to 34.6 GPa (see Fig. 8a) also exhibit a pressure-induced increase in the relative intensity of the $^6P_{7/2} \rightarrow {}^8S_{7/2}$-related peak and decrease in intensity of the $4f^6 5d^1 \rightarrow 4f^7({}^8S_{7/2})$ band. As depicted in **Fig. 8b**, the peak centroid of the $^6P_{7/2} \rightarrow {}^8S_{7/2}$ transition continuously shifts to red with increasing pressure at the same rate (0.17 nm/GPa) as in the case of lower Eu^{2+} doping concentrations. Hence, the dopant concen-
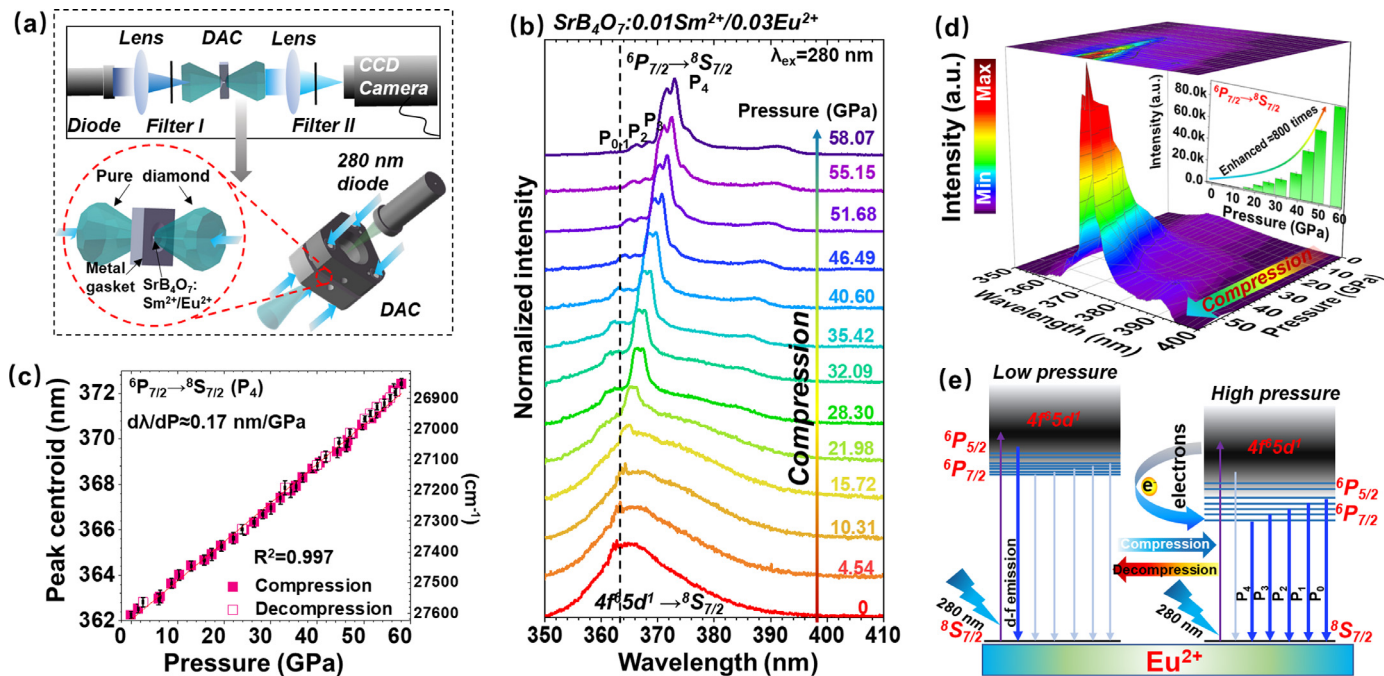
Fig. 7. a) Schematic configuration of a diamond anvil cell (DAC) and the experimental setup used for high-pressure luminescence measurements. Filter *I* and *II* is the optical short pass filter and long pass filter, respectively. b) Selected, normalized UV emission spectra of the SrB_4O_7: 0.03Eu^{2+}, 0.01Sm^{2+} material, measured with increasing pressure values. c) Spectral position (peak centroid) of the P_4 component of $4f^7 \rightarrow 4f^7$ transition of Eu^{2+}. d) Non-normalized UV emission spectra measured at increasing pressure values; the inset presents the integrated intensity of the $4f^7({}^6P_{7/2}) \rightarrow 4f^7({}^8S_{7/2})$ emission as a function of pressure. e) A simplified diagram of the energy levels for Eu^{2+} in the SrB_4O_7 matrix at low and high pressure conditions.
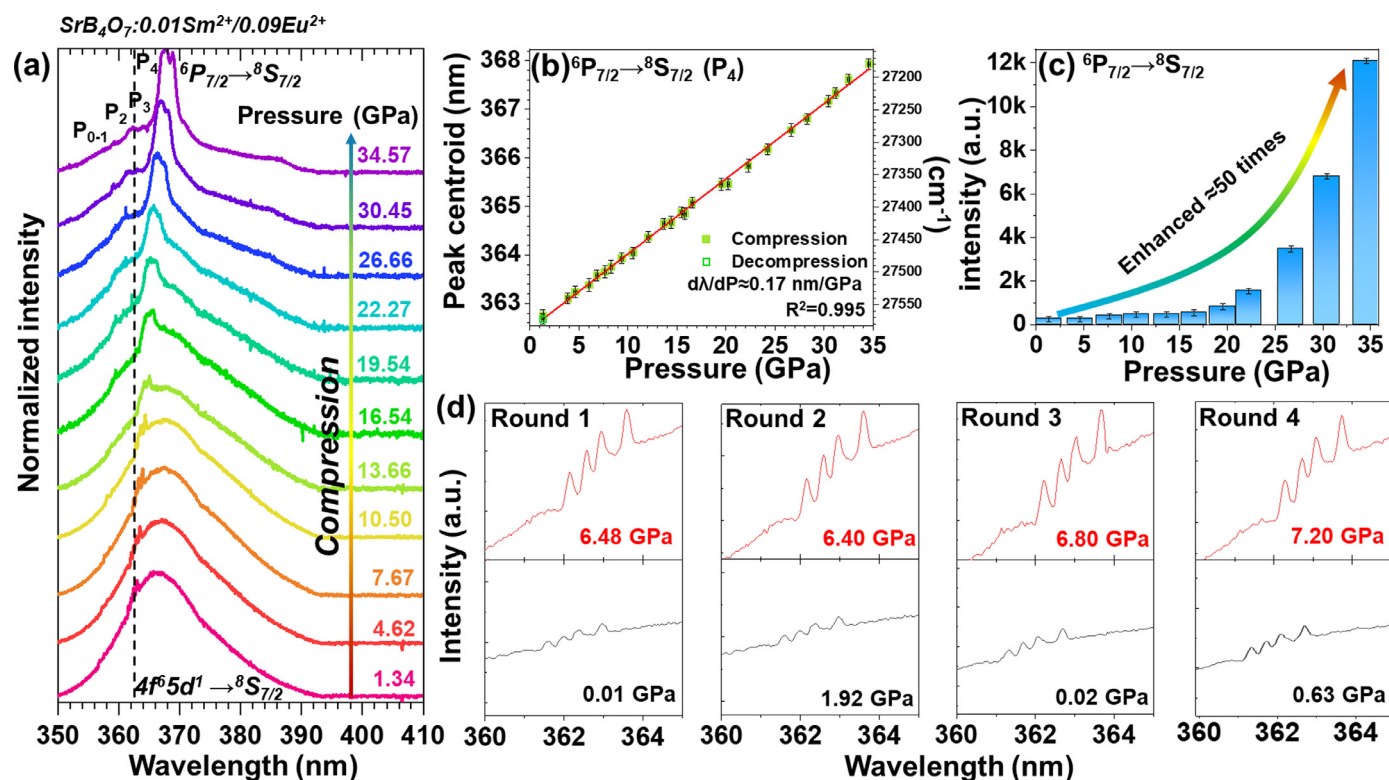
Fig. 8. (a) Selected, normalized UV emission spectra of SrB_4O_7: 0.09 Eu^{2+}, 0.01Sm^{2+} measured at increasing pressure values and room temperature. (b) Spectral position (peak centroid) of the P_4 components of the $4f^7(^6P_{7/2})$- $4f^7(^8S_{7/2})$ transition of Eu^{2+}. (c) Integrated intensity of the $^6P_{7/2} \rightarrow {}^8S_{7/2}$ ($4f^7 \rightarrow 4f^7$) emission as a function of pressure. (d) Magnified emission spectra, emphasizing the $^6P_{7/2} \rightarrow {}^8S_{7/2}$ transition, recorded during four different compression cycles.

tration has a negligible influence on the shift rate of this narrow emission band. If the pressure is higher than 20 GPa, the $4f^65d^1 \rightarrow 4f^7(^8S_{7/2})$ broad-band emission practically disappears, and the $4f^7(^6P_{7/2}) \rightarrow 4f^7(^8S_{7/2})$ luminescence completely dominates the luminescence spectrum. As shown in Fig. 8**c**, the absolute intensity of the P_4 peak of the $4f^7(^6P_{7/2}) \rightarrow 4f^7(^8S_{7/2})$ emission at 34.6 GPa is about 50 times higher than at 1.3 GPa. It is important to mention that these effects were observed in four independent compression-decompression experiments (cycles), as shown in Fig. 8**d**, confirming the reliability of our experiments and the reversibility of the observed effects.

These results show that pressure acts inversely to temperature, *i.e.*, deteriorating the intensity of the $4f^65d^1$-$4f^7$ emission and enhancing the $4f^7(^6P_{7/2}) \rightarrow 4f^7(^8S_{7/2})$ luminescence. Due to the fact that the Eu^{2+} emission intensity is higher in the sample with 9 mol% of Eu^{2+} (see **Fig. S1a)**, we calculated the pressure shift rate of the $4f^65d^1 \rightarrow 4f^7(^8S_{7/2})$ band for this sample. As shown in **Fig. S9** in the SI, the pressure-induced shift of the interconfigurational, parity-allowed $4f^65d^1 \rightarrow 4f^7(^8S_{7/2})$ transition is estimated to be around -8.5 cm^{-1}/GPa (0.11 nm/GPa), which is lower compared to the shift of the $4f^7(^6P_{7/2}) \rightarrow 4f^7(^8S_{7/2})$ emission (-12.84 cm^{-1}/GPa; 0.17 nm/GPa). That is why the energy separation of the excited $4f^65d$ configuration and the $^6P_{7/2}$ emitting levels appears to change with pressure, leading to a decreasing intensity of the $4f^65d^1 \rightarrow 4f^7(^8S_{7/2})$ broad band with increasing pressure and complete quenching above $\approx$ 35GPa. Phonon energies and electron-phonon coupling increase with pressure, which can be observed in the Raman spectra and the vibronic bands at the high energy side of the $4f^7(^6P_{7/2}) \rightarrow 4f^7(^8S_{7/2})$ emission peaks. However, these two effects do not have a dominant impact on the intensity of the discussed $4f^7 \rightarrow 4f^7$ transitions of Eu^{2+}, which is significantly enhanced with increasing pressure.

The centroid red-shift of the $^6P_{7/2} \rightarrow {}^8S_{7/2}$ can be additionally explained by an increase in the nephelauxetic effect: the interelectronic repulsion decreases as the shorter Eu-O bond lengths also lead to a higher covalent nature of the bond. Correspondingly, the Slater-Condon-Shortley parameters expectedly decrease, which determine the energy of the excited $4f^7$ states relative to the ground level in general. As the mutual electron repulsion among the 4f electrons is reduced in the more extended, lower valent Eu^{2+} ion, the energy of the higher excited $^6P_{7/2}$ levels is reduced. Concerning the fact that the narrow $4f^7 \rightarrow 4f^7$-related luminescence becomes dominant at elevated pressures, it is actually an indication that the bond length in the lowest excited $4f^65d^1$ state must be smaller than in the $^8S_{7/2}$ ground level. The concept is demonstrated schematically in Fig. 9. It turns out that for a bond-contracted $4f^65d^1$ state, elevation of pressure will lead to a higher thermal activation barrier to thermally populate the lowest excited $4f^65d^1$ state. Such a bond contraction in the lowest excited $4f^65d^1$ level has been consistently proven for several trivalent and divalent lanthanides [112–114]. In contrast, an elongated bond in the excited $4f^65d^1$ state would actually lead to an even more dominant $4f^65d^1 \rightarrow 4f^7$ broad-band emission at higher pressure. The significant enhancement in the narrow $4f^7 \rightarrow 4f^7$-related luminescence is thus a consequence of the reduced non-radiative thermal crossover to the excited $4f^65d^1$ state (see Fig. 9**a and b**).

As shown in Figs. 7**b and** 8**a**, in the initial pressure stages, the $4f^7 \rightarrow 4f^7$ emission lines broaden and overlap, and, at HP, the splitting of the peaks increases with increasing pressure, indicating a stronger magnitude of the crystal-field interaction acting on the Eu^{2+} ions when the volume of the [EuO_9] polyhedron decreases with pressure. However, as already indicated above, the Eu^{2+} ion in the SrB_4O_7 structure is only prone to a rather weak crystal field and very ionic bonds to the surrounding oxygen atoms.
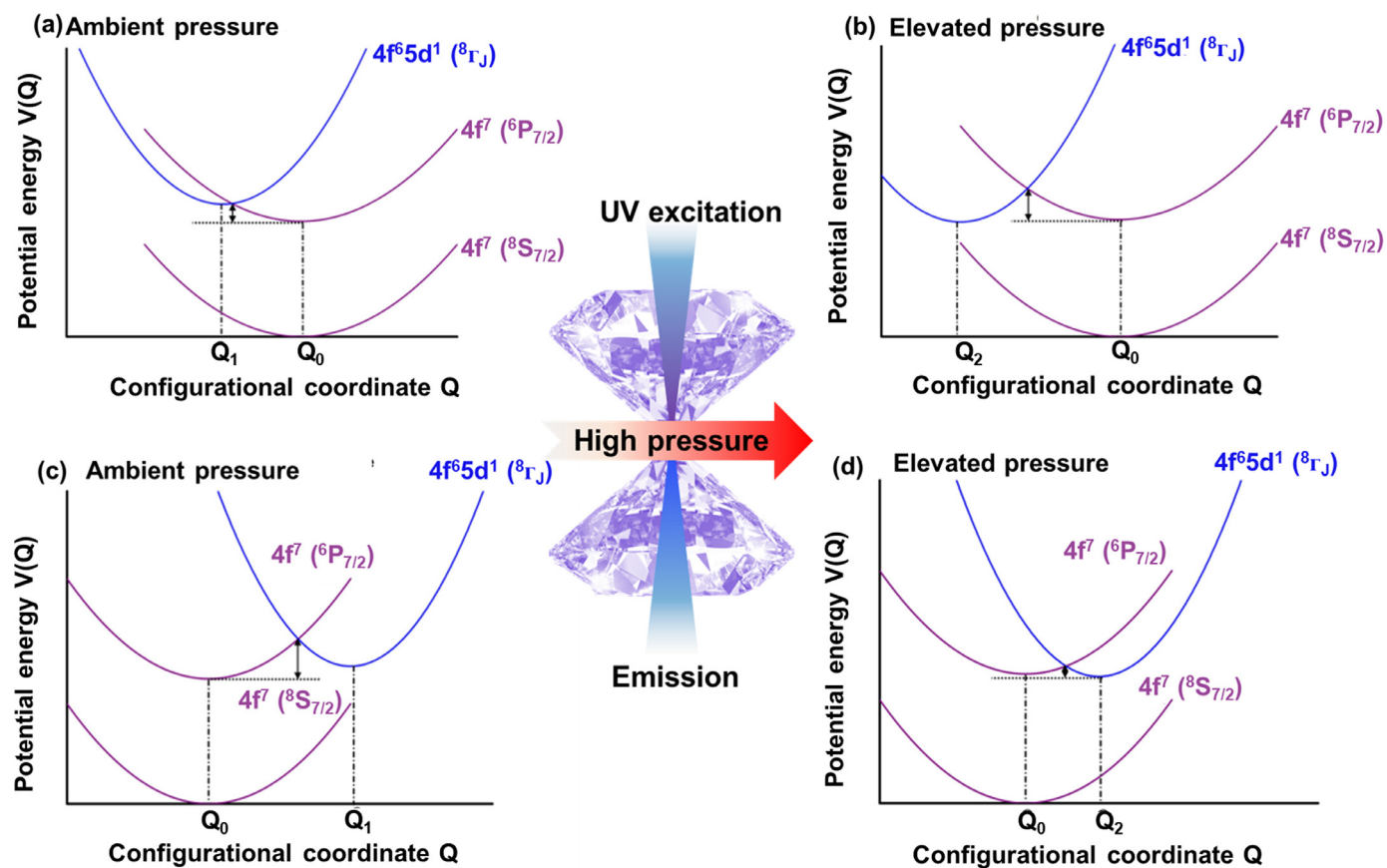
Fig. 9. (a) Impact of the position of the lowest excited $4f^6 5d^1$ state relative to the $^6P_{7/2}$ level of Eu^{2+} in the configurational coordinate space on the appearance of the respective luminescence spectrum; (b) shows the case of a bond contraction upon excitation into the $4f^6 5d^1$ state; while (c) and (d) show the pressure dependence if the excited $4f^6 5d^1$ state has higher equilibrium bond distances.

Since the pressure strongly reduces the volume of the [EuO$_9$] entity, the crystal-field interaction should increase. Anyway, the large volume changes of the [EuO$_9$] polyhedron may be responsible for relatively large changes in the red-shift of the luminescence. When Eu^{2+} is incorporated in the SrB_4O_7 network, the contraction of energy differences between multiplets is more important than the increase in individual splitting of each multiplet due to crystal-field interaction, indicating the importance of pressure-induced changes in the covalency nature of the Eu^{2+} local environment [109,110]. The quantum efficiency of the emission from the $^6P_{7/2}$ multiplet is practically 100% given the large gap to the ground multiplet that makes multiphonon relaxation improbable. The proximity of the $^6P_{7/2}$ Stark levels and the lowest $4f^6 5d^1$ multiplets of the excited configuration and the increasing odd part of the crystal-field interaction with the pressure favor this mixing. This, in turn, gives rise to an increase of the parity-allowed components of the $^6P_{7/2}$ levels and, thus, increasing the spontaneous emission probabilities of the $4f^7(^6P_{7/2}) \rightarrow 4f^7(^8S_{7/2})$ transitions over the inter-configurational emission. Since vibronic transitions involve electronic and phonon states, they are also enhanced by pressure.

In Table S7, we summarize and compare the extraordinary pressure sensing performance of the studied material with the other optical pressure gauges reported. The Eu^{2+} and Sm^{2+} co-doped SrB_4O_7 pressure sensor shows its superiority as a high-accuracy and high-precision, reversible pressure gauge, operating within a very wide pressure range. The spectral shift of the narrow $4f^7(^6P_{7/2}) \rightarrow 4f^7(^8S_{7/2})$ emission line can be applied as a manometric parameter, when experiments require compression under very high pressure conditions (*i.e.*, above ≈ 30 GPa). This is due to the great advantage of its pressure-enhanced signal intensity, narrow emission line, and significant and reversible spectral shift, as well as negligible temperature dependence.

5. Conclusions

A strong pressure-induced enhancement of the $4f^7(^6P_{7/2}) \rightarrow 4f^7(^8S_{7/2})$ emission intensity of Eu^{2+} was recorded in SrB_4O_7 for the first time. In order to investigate and support the proposed mechanism underlying the pressure-dependent photoluminescence, a combination of theoretical and experimental studies of the structural, vibrational, elastic, and luminescence properties was systematically performed on SrB_4O_7:Eu^{2+} at varying pressure and temperature. It could be established that the strong enhancement of the intensity of the $4f^7(^6P_{7/2}) \rightarrow 4f^7(^8S_{7/2})$ emission intensity is a pressure-induced configuration crossover between the energetically close $4f^7(^6P_{7/2})$ and $4f^6 5d^1$ excited configurations. It turns out that elevated pressure has the opposite effect on the appearance of the luminescence spectra to temperature and favors the narrow line emission. In contrast to the currently applied sensors, usually showing a significant luminescence quenching (signal deterioration) under high-pressure conditions, the narrow emission lines of Eu^{2+} show a strong increase in the intensity of the obtained material, as well as a significant spectral shift ($\sim$ -12.84 cm^{-1}/GPa) alongside with negligible temperature dependence. Such a co-doped (Eu^{2+}/Sm^{2+}) luminescent material SrB_4O_7 can be applied as a multi-mode, pressure-enhanced gauge, which offers new perspectives for research under high-pressure conditions.

Data availability

The original data for this study are available from the corresponding authors upon request.

Fourier transform infrared (FTIR) spectrpscopy of these catalysts were conducted on a Thermo Scientific Nicolet Is5 spectrometer using KBr pellet technique.

Declaration of Competing Interest

The authors declare that they have no known competing financial interests or personal relationships that could have appeared to influence the work reported in this paper.

Acknowledgements

Supplementary materials

Supplementary material associated with this article can be found, in the online version, at doi:10.1016/j.actamat.2022.117886.

References

[1] S. Liu, S. Sun, C.K. Gan, A.G. Del Águila, Y. Fang, J. Xing, T.Thu Ha Do, T.J. White, H. Li, W. Huang, Q. Xiong, Manipulating efficient light emission in two-dimensional perovskite crystals by pressure-induced anisotropic deformation, Sci. Adv. 5 (2019) 1–11, doi:10.1126/sciadv.aav9445.

[2] J. Sun, Q. Li, H. Zhu, Z. Liu, K. Lin, N. Wang, Q. Zhang, L. Gu, J. Deng, J. Chen, X. Xing, Negative-pressure-induced large polarization in Nanosized $PbTiO_3$, Adv. Mater. 32 (2020) 1–6, doi:10.1002/adma.202002968.

[3] H. Liu, Y. Gu, Y. Dai, K. Wang, S. Zhang, G. Chen, B. Zou, B. Yang, Pressure-induced blue-shifted and enhanced emission: a cooperative effect between aggregation-induced emission and energy-transfer suppression, J. Am. Chem. Soc. 142 (2020) 1153–1158, doi:10.1021/jacs.9b11080.

[4] M. Runowski, P. Woźny, S. Lis, V. Lavín, I.R. Martín, Optical vacuum sensor based on lanthanide Upconversion—luminescence thermometry as a tool for ultralow pressure sensing, Adv. Mater. Technol. 5 (2020) 1901091, doi:10.1002/admt.201901091.

[5] X. Liu, W. Xie, Y. Lü, J. Feng, X. Tang, J. Lin, Y. Dai, Y. Xie, L. Yan, Multichannel luminescence properties of mixed-valent Eu^{2+}/Eu^{3+} coactivated $SrAl_3BO_7$ nanocrystalline phosphors for Near-UV LEDs, Inorg. Chem. 56 (2017) 13829–13841, doi:10.1021/acs.inorgchem.7b01938.

[6] J.A. Sans, V. Monteseguro, G. Garbarino, M. Gich, V. Cerantola, V. Cuartero, M. Monte, T. Irifune, A. Muñoz, C. Popescu, Stability and nature of the volume collapse of ε-Fe_2O_3 under extreme conditions, Nat. Commun. 9 (2018) 4554, doi:10.1038/s41467-018-06966-9.

[7] D. Santamaria-Perez, C. McGuire, A. Makhluf, A. Kavner, R. Chuliá-Jordan, J.L. Jorda, F. Rey, J. Pellicer-Porres, D. Martinez-García, P. Rodriguez-Hernandez, A. Muñoz, Correspondence: strongly-driven $Re+CO_2$ redox reaction at high-pressure and high-temperature, Nat. Commun. 7 (2016) 4–6, doi:10.1038/ncomms13647.

[8] D.A. Davis, A. Hamilton, J. Yang, L.D. Cremar, D. Van Gough, S.L. Potisek, M.T. Ong, P.V. Braun, T.J. Martínez, S.R. White, J.S. Moore, N.R. Sottos, Force-induced activation of covalent bonds in mechanoresponsive polymeric materials, Nature 459 (2009) 68–72, doi:10.1038/nature07970.

[9] Y. Wang, X. Tan, Y.M. Zhang, S. Zhu, I. Zhang, B. Yu, K. Wang, B. Yang, M. Li, B. Zou, S.X.A. Zhang, Dynamic behavior of molecular switches in crystal under pressure and its reflection on tactile sensing, J. Am. Chem. Soc. 137 (2015) 931–939, doi:10.1021/ja511499p.

[10] X. Jiang, Y. Yang, M.S. Molokeev, P. Gong, F. Liang, S. Wang, L. Liu, X. Wu, X. Li, Y. Li, S. Wu, W. Li, Y. Wu, Z. Lin, Zero linear compressibility in Non-dense borates with a "Lu-Ban Stool"-Like structure, Adv. Mater. 30 (2018) 1–7, doi:10.1002/adma.201801313.

[11] X. Jiang, M.S. Molokeev, L. Dong, Z. Dong, N. Wang, L. Kang, X. Li, Y. Li, C. Tian, S. Peng, W. Li, Z. Lin, Anomalous mechanical materials squeezing three-dimensional volume compressibility into one dimension, Nat. Commun. 11 (2020) 1–7, doi:10.1038/s41467-020-19219-5.

[12] Y.N. Zhuravlev, V.V. Atuchin, First-principle studies of the vibrational properties of carbonates under pressure, Sensors 21 (2021), doi:10.3390/s21113644.

[13] M.A. Antoniak, S.J. Zelewski, R. Oliva, A. Żak, R. Kudrawiec, M. Nyk, Combined Temperature and Pressure Sensing Using Luminescent $NaBiF_4$:Yb,Er Nanoparticles, ACS Appl. Nano Mater. 3 (2020) 4209–4217, doi:10.1021/acsanm.0c00403.

[14] R.A. Forman, G.J. Piermarini, J.Dean Barnett, S. Block, Pressure measurement made by the utilization of ruby sharp-line luminescence, Science 80 (176) (1972) 284–285, doi:10.1126/science.176.4032.284.

[15] A. Lacam, C. Chateau, High-pressure measurements at moderate temperatures in a diamond anvil cell with a new optical sensor: SrB_4O_7:Sm^{2+}, J. Appl. Phys. 66 (1989) 366–372, doi:10.1063/1.343884.

[16] Z. Dai, J. Xie, W. Liu, X. Wang, L. Zhang, Z. Zhou, J. Li, X. Ren, Effective strategy to achieve excellent energy storage properties in Lead-Free $BaTiO^3$-based bulk ceramics, ACS Appl. Mater. Interfaces. 12 (2020) 30289–30296, doi:10.1021/acsami.0c02832.

[17] S. Goderski, M. Runowski, P. Woźny, V. Lavín, S. Lis, Lanthanide Upconverted luminescence for simultaneous contactless optical thermometry and manometry-sensing under extreme conditions of pressure and temperature, ACS Appl. Mater. Interfaces. 12 (2020) 40475–40485, doi:10.1021/acsami.0c09882.

[18] M. Zhao, Q. Zhang, Z. Xia, Structural engineering of Eu^{2+}-doped silicates phosphors for LED applications, Accounts Mater. Res. 1 (2020) 137–145, doi:10.1021/accountsmr.0c00014.

[19] G.J. Hoerder, M. Seibald, D. Baumann, T. Schröder, S. Peschke, P.C. Schmid, T. Tyborski, P. Pust, I. Stoll, M. Bergler, C. Patzig, S. Reißaus, M. Krause, L. Berthold, T. Höche, D. Johrendt, H. Huppertz, $Sr[Li_2Al_2O_2N_2]$:Eu^{2+} —A high performance red phosphor to brighten the future, Nat. Commun. 10 (2019) 1–9, doi:10.1038/s41467-019-09632-w.

[20] P. Pust, V. Weiler, C. Hecht, A. Tücks, A.S. Wochnik, A.K. Henß, D. Wiechert, C. Scheu, P.J. Schmidt, W. Schnick, Narrow-band red-emitting $Sr[LiAl_3N_4]$:Eu^{2+} as a next-generation LED-phosphor material, Nat. Mater. 13 (2014) 891–896, doi:10.1038/nmat4012.

[21] T. Zheng, M. Runowski, P. Woźny, S. Lis, Influence of matrix on the luminescence properties of Eu^{2+}/Eu^{3+} doped strontium borates: SrB_4O_7, SrB_2O_4 and $Sr_3(BO_3)_2$, exhibiting multicolor tunable emission, J. Alloys Compd. 822 (2020) 1–9, doi:10.1016/j.jallcom.2019.153511.

[22] J. Zhang, R. Li, Q. Chen, G. Zhao, J. Jia, Porous carbon-coated Li_2MoO_4 as high-performance anode materials for lithium-ion batteries, Mater. Lett. 233 (2018) 302–305, doi:10.1016/j.matlet.2018.09.032.

[23] J. Qiao, G. Zhou, Y. Zhou, Q. Zhang, Z. Xia, Divalent europium-doped near-infrared-emitting phosphor for light-emitting diodes, Nat. Commun. 10 (2019) 1–7, doi:10.1038/s41467-019-13293-0.

[24] G. Li, C.C. Lin, W.T. Chen, M.S. Molokeev, V.V. Atuchin, C.Y. Chiang, W. Zhou, C.W. Wang, W.H. Li, H.S. Sheu, T.S. Chan, C. Ma, R.S. Liu, Photoluminescence tuning via cation substitution in oxonitridosilicate phosphors: DFT calculations, different site occupations, and luminescence mechanisms, Chem. Mater. 26 (2014) 2991–3001, doi:10.1021/cm500844v.

[25] Z. Xia, Y. Zhang, M.S. Molokeev, V.V. Atuchin, Y. Luo, Linear structural evolution induced tunable photoluminescence in clinopyroxene solid-solution phosphors, Sci. Rep. 3 (2013) 1–7, doi:10.1038/srep03310.

[26] J. Ueda, J. Wylezich, N. Kunkel, S. Tanabe, Red luminescent Eu^{2+} in K_2MgH_4 and comparison with $KMgH_3$, J. Mater. Chem. C. 8 (2020) 5124–5130, doi:10.1039/c9tc06459a.

[27] H. Ji, Z. Huang, Z. Xia, M.S. Molokeev, V.V. Atuchin, M. Fang, Y. Liu, Discovery of new solid solution phosphors via cation substitution-dependent phase transition in $M_3(PO_4)_2$:Eu^{2+} (M = Ca/Sr/Ba) quasi-binary sets, J. Phys. Chem. C. 119 (2015) 2038–2045, doi:10.1021/jp509743r.

[28] A. Baran, S. Mahlik, M. Grinberg, E. Zych, High pressure and time-resolved luminescence spectra of $Ca_3Y_2(SiO_4)_3$ doped with Eu^{2+} and Eu^{3+}, J. Phys. Condens. Matter. (2013) 25, doi:10.1088/0953-8984/25/2/025603.

[29] K. Winskiewski, S. Mahlik, M. Grinberg, H.J. Seo, Influence of high hydrostatic pressure on Eu^{2+}-luminescence in $KMgF_3$:Eu^{2+} crystal, J. Lumin. 131 (2011) 306–309, doi:10.1016/j.jlumin.2010.10.020.

[30] R.A. Hewes, M.V Hoffman, G.E. Company, $4f^7$-$4f^7$ Emission from Eu^{2+} system MF_2•AlF_3, J. Lumin. 3 (2000) 261–280.

[31] C. Helvacı, Occurrence of rare borate minerals: Veatchite-A, tunellite, terug-gite and cahnite in the Emet borate deposits, Turkey, Miner. Depos. 19 (1984) 217–226, doi:10.1007/BF00199788.

[32] M. Mohapatra, B. Rajeswari, R.M. Kadam, M. Kumar, T.K. Seshagiri, N.K. Porwal, S.V. Godbole, V. Natarajan, Investigation of uranium luminescence in SrB_4O_7 matrix by time resolved photoluminescence, thermally stimulated luminescence and electron spin resonance spectroscopy, J. Alloys Compd. 611 (2014) 74–81, doi:10.1016/j.jallcom.2014.05.096.

[33] J. Sun, J. Zhu, X. Liu, H. Du, Luminescence properties of $SrB_4O_7:Sm^{2+}$ for light conversion agent, J. Rare Earths. 30 (2012) 1084–1087, doi:10.1016/S1002-0721(12)60183-5.

[34] C.B. Palan, N.S. Bajaj, S.K. Omanwar, Luminescence properties of Eu^{2+} doped SrB_4O_7 phosphor for radiation dosimetry, Mater. Res. Bull. 76 (2016) 216–221, doi:10.1016/j.materresbull.2015.12.027.

[35] V.V. Atuchin, V.G. Kesler, A.I. Zaitsev, M.S. Molokeev, A.S. Aleksandrovsky, A.A. Kuzubov, N.Y. Ignatova, Electronic structure of α-SrB_4O_7: experiment and theory, J. Phys. Condens. Matter. (2013) 25, doi:10.1088/0953-8984/25/8/085503.

[36] H. Huppertz, High-pressure preparation, crystal structure, and properties of $RE_4B_6O_{15}$ (RE = Dy, Ho) with an extension of the "fundamental building block"-descriptors, Zeitschrift Fur Naturforsch. - Sect. B J. Chem. Sci. 58 (2003) 278–290, doi:10.1515/znb-2003-0406.

[37] K. Machida, G. Adachi, J. Shiokawa, Luminescence properties of Eu(II)-borates and Eu^{2+}- activated Sr-Borates, J. Lumin. 21 (1979) 101–110, doi:10.1016/0022-2313(79)90038-3.

[38] A. Meijerink, J. Nuyten, G. Blasse, Luminescence and energy migration in $(Sr,Eu)B_4O_7$, a system with a $4f^7$-$4f^65d$ crossover in the excited state, J. Lumin. 44 (1989) 19–31, doi:10.1016/0022-2313(89)90017-3.

[39] T. Zheng, M. Runowski, P. Woźny, S. Lis, V. Lavín, Huge enhancement of Sm^{2+} emission: Via Eu^{2+} energy transfer in a SrB_4O_7 pressure sensor, J. Mater. Chem. C. 8 (2020) 4810–4817, doi:10.1039/d0tc00463d.

[40] P. Hohenberg, Inhomogeneous electron gas, Phys. Rev. 9 (1964) 864–871, doi:10.1007/BF01198136.

[41] G. Kresse, J. Hafner, Ab initio molecular dynamics for liquid metals, Phys. Rev. B. 47 (1993) 558–561, doi:10.1103/PhysRevB.47.558.

[42] D. Joubert, From ultrasoft pseudopotentials to the projector augmented-wave method, Phys. Rev. B - Condens. Matter Mater. Phys. 59 (1999) 1758–1775, doi:10.1103/PhysRevB.59.1758.

[43] J.P. Perdew, A. Ruzsinszky, G.I. Csonka, O.A. Vydrov, G.E. Scuseria, L.A. Constantin, X. Zhou, K. Burke, Restoring the density-gradient expansion for exchange in solids and surfaces, Phys. Rev. Lett. 100 (2008) 1–4, doi:10.1103/PhysRevLett.100.136406.

[44] K. Hu, M. Wu, S. Hinokuma, T. Ohto, M. Wakisaka, J.I. Fujita, Y. Ito, Boosting electrochemical water splitting: via ternary NiMoCo hybrid nanowire arrays, J. Mater. Chem. A. 7 (2019) 2156–2164, doi:10.1039/c8ta11250a.

[45] N. Chetty, A. Muoz, R.M. Martin, First-principles calculation of the elastic constants of AlAs, Phys. Rev. B. 40 (1989) 11934–11936, doi:10.1103/PhysRevB.40.11934.

[46] O.H. Nielsen, R.M. Martin, Quantum-mechanical theory of stress and force, Phys. Rev. B. 32 (1985) 3780–3791, doi:10.1103/PhysRevB.32.3780.

[47] Y.Le Page, P. Saxe, Symmetry-general least-squares extraction of elastic data for strained materials from ab initio calculations of stress, Phys. Rev. B - Condens. Matter Mater. Phys. 65 (2002) 1–14, doi:10.1103/PhysRevB.65.104104.

[48] A. Perloff, S. Block, The crystal structure of the strontium and lead tetraborates, $Sr_{0.2}B_2O_3$ and $Pb_{0.2}B_2O_3$, Acta Crystallogr 20 (1966) 274–279, doi:10.1107/s0365110x66000525.

[49] F. Pan, G. Shen, R. Wang, X. Wang, D. Shen, Growth, characterization and nonlinear optical properties of SrB_4O_7 crystals, J. Cryst. Growth. 241 (2002) 108–114, doi:10.1016/S0022-0248(02)00873-4.

[50] B.Y.K. Machida, G. Adachi, J. Shiokawa, Structure of Europium (II) Tetraborate, (2008) 2008–2011.

[51] D.L. Pye, D.V. Fréchette, N.J. Kreidl, Borate Glasses: Structure, Properties, Applications, Springer, 2021 n.d., doi:10.1007/978-1-4684-3357-9.

[52] G. Blasse, G.J. Dirksen, A. Meijerink, The luminescence of ytterbium(II) in Strontium tetraborate, Chem. Phys. Lett. 167 (1989) 41–44.

[53] Z. Pei, Q. Su, J. Zhang, The valence change from RE^{3+} SrB_4O_7: RE prepared in air and to RE^{2+} (RE = Eu, Sm, Yb) in the spectral properties of RE^{2+}, J. Alloys Compd. 198 (1993) 51–53.

[54] A.A.B.B. Baloch, S.M. Alqahtani, F. Mumtaz, A.H. Muqaibel, S.N. Rashkeev, F.H. Alharbi, Extending Shannon's ionic radii database using machine learning, Phys. Rev. Mater. 5 (2021) 1–10, doi:10.1103/PhysRevMaterials.5.043804.

[55] J.F. Nye, Physical properties of crystals: their representation by tensors and matrices, n.d. https://books.google.ie/books/about/Physical_Properties_of_Crystals.html?id=ugwql-uVB44C&redir_esc=y (accessed January 28, 2021).

[56] I. Martynyuk-Lototska, T. Dudok, O. Mys, R. Vlokh, Elastic, piezoelectric and acoustooptic properties of SrB_4O_7 and PbB_4O_7 crystals, Opt. Mater. (Amst). 31 (2009) 660–667, doi:10.1016/j.optmat.2008.06.020.

[57] V.I. Zinenko, M.S. Pavlovskii, A.I. Zaitzev, A.S. Krylov, A.S. Shinkorenko, Vibrational spectra and elastic piezoelectric and polarization properties of the α-SrB_4O_7 crystal, J. Exp. Theor. Phys. 115 (2012) 455–461, doi:10.1134/S1063776112080195.

[58] K. Babesse, D. Hammoutène, P. Rodríguez-Hernández, A. Muñoz, K. Kassali, R. Nedjar, High pressure study of structural, electronic, elastic, and vibrational properties of $NaNb_3O_8$, J. Alloys Compd. 725 (2017) 773–782, doi:10.1016/j.jallcom.2017.07.231.

[59] W. Voigt, Lehrbuch der Kristallphysik, 1966. doi:10.1007/978-3-663-15884-4.

[60] A. Reuss, Berechnung der Fließgrenze von Mischkristallen auf Grund der Plastizitätsbedingung für Einkristalle. ZAMM - J. Appl. Math. Mech. /Zeitschrift Für Angew. Mat, h. Und Mech. 9 (1929) 49–58, doi:10.1002/zamm.19290090104.

[61] R. Hill, The elastic behaviour of a crystalline aggregate, Proc. Phys. Soc. Sect. A. 65 (1952) 349–354, doi:10.1088/0370-1298/65/5/307.

[62] F. Birch, Finite elastic strain of cubic crystals, Phys. Rev. 71 (1947) 809–824, doi:10.1103/PhysRev.71.809.

[63] S.F. Pugh XCII, Relations between the elastic moduli and the plastic properties of polycrystalline pure metals, London, Edinburgh, Dublin Philos. Mag. J. Sci. 45 (1954) 823–843, doi:10.1080/14786440808520496.

[64] V. Tvergaard, John W. Hutchinson, Microcracking in ceramics induced by thermal expansion or elastic anisotropy, J. Am. Ceram. Soc. 71 (1988) 157–166, doi:10.1111/j.1151-2916.1988.tb05022.x.

[65] S.I. Ranganathan, M. Ostoja-Starzewski, Universal elastic anisotropy index, Phys. Rev. Lett. 101 (2008) 3–6, doi:10.1103/PhysRevLett.101.055504.

[66] E. Schreiber, O.L. Anderson, N. Soga, J.F. Bell, Elastic constants and their measurement, 1975. doi:10.1115/1.3423687.

[67] O.L. Anderson, A simplified method for calculating the debye temperature from elastic constants, J. Phys. Chem. Solids. 24 (1963) 909–917, doi:10.1016/0022-3697(63)90067-2.

[68] X. Qin, X. Liu, W. Huang, M. Bettinelli, X. Liu, Lanthanide-activated phosphors based on 4f-5d optical transitions: theoretical and experimental aspects, Chem. Rev. 117 (2017) 4488–4527, doi:10.1021/acs.chemrev.6b00691.

[69] A.A. Sobol, V.E. Shukshin, A.I. Zaitsev, Raman spectroscopy of SrB_4O_7 single crystals in the temperature range 300–1273 K, Opt. Spectrosc. 121 (2016) 25–31, doi:10.1134/S0030400x16070201.

[70] J. Hanuza, J.Lorenc M.Mączka, A.A. Kaminskii, P. Becker, L. Bohatý, Recent Advances in linear and nonlinear Raman spectroscopy I, J. Raman Spectrosc. 38 (2007) 1538–1553, doi:10.1002/jrs.

[71] A.A. Sobol, V.E. Shukshin, L.V. Moiseeva, Study of Raman spectra in the processes of glass formation, crystallization, and melting of strontium diborate, Opt. Spectrosc. (English Transl. Opt. i Spektrosk. 121 (2016) 32–35, doi:10.1134/S0030400x16070213.

[72] A.L.D.J. Pereira, D. Santamariá-Pérez, R. Vilaplana, D. Errandonea, C. Popescu, E.L. Da Silva, J.A. Sans, J. Rodríguez-Carvajal, A. Munõz, P. Rodríguez-Hernández, A. Mujica, S.E. Radescu, A. Beltrán, A. Otero-De-La-Roza, M. Nalin, M. Mollar, F.J. Manjón, Experimental and theoretical study of $SbPO_4$ under compression, Inorg. Chem. 59 (2020) 287–307, doi:10.1021/acs.inorgchem.9b02268.

[73] D. Errandonea, O. Gomis, P. Rodriguez-Hernández, A. Munz, J. Ruiz-Fuertes, M. Gupta, S.N. Achary, A. Hirsch, F.J. Manjon, L. Peters, G. Roth, A.K. Tyagi, M. Bettinelli, High-pressure structural and vibrational properties of monazite-type $BiPO_4$, $LaPO_4$, $CePO_4$, and $PrPO_4$, J. Phys. Condens. Matter. 30 (2018) 065401, doi:10.1088/1361-648X/aaa20d.

[74] J.H. Denning, S.D. Ross, Speotra and Struotures, Spectrochim. Acta. 28A (1984) 1775–1785.

[75] S.D. Ross, The vibrational spectra of some minerals containing tetrahedrally co-ordinated boron, Spectrochim. Acta Part A Mol. Spectrosc. 28 (1972) 1555–1561, doi:10.1016/0584-8539(72)80126-0.

[76] S.D. Ross, Vibrational assignments in borates with the vaterite structure, J. Mol. Spectrosc. 29 (1969) 131–145, doi:10.1016/0022-2852(69)90093-9.

[77] F. Auzel, Upconversion and Anti-Stokes Processes with f and d Ions in Solids, Chem. Rev. 104 (2004) 139–173, doi:10.1021/cr020357g.

[78] J. Zhou, Q. Liu, W. Feng, Y. Sun, F. Li, Upconversion luminescent materials: advances and applications, Chem. Rev. 115 (2015) 395–465, doi:10.1021/cr400478f.

[79] F.M. Ryan, W. Lehmann, D.W. Feldman, J. Murphy, Fine structure in the optical spectra of divalent europium in the alkaline earth sulfates, J. Electrochem. Soc. 121 (1974) 1475, doi:10.1149/1.2401714.

[80] Y. Huang, J. Qin, Z. Fan, D. Wei, H.J. Seo, Photoenergy conversion behaviors of photoluminescence and photocatalysis in Silver-Coated $LiBaPO_4:Eu^{2+}$, Inorg. Chem. 58 (2019) 13161–13169, doi:10.1021/acs.inorgchem.9b02037.

[81] J. Xiang, J. Zheng, Z. Zhou, H. Suo, X. Zhao, X. Zhou, N. Zhang, M.S. Molokeev, C. Guo, Enhancement of red emission and site analysis in Eu^{2+} doped new-type structure $Ba_3CaK(PO_4)_3$ for plant growth white LEDs, Chem. Eng. J. 356 (2019) 236–244, doi:10.1016/j.cej.2018.09.036.

[82] C.E. Tyner, H.G. Drickamer, Studies of luminescence efficiency of Eu^{2+} activated phosphors as a function of temperature and high pressure, J. Chem. Phys. 67 (1977) 4116–4123, doi:10.1063/1.435388.

[83] N. Yamashita, Coexistence of the Eu^{2+} and Eu^{3+} centers in the CaO : Eu powder phosphor, J. Electrochem. Soc. 140 (1993) 840–843, doi:10.1149/1.2056169.

[84] R.P. Yavetskiy, E.F. Dolzhenkova, A.V. Tolmachev, S.V. Parkhomenko, V.N. Baumer, A.L. Prosvirnin, Radiation defects in $SrB_4O_7:Eu^{2+}$ crystals, J. Alloys Compd. 441 (2007) 202–205, doi:10.1016/j.jallcom.2006.09.077.

[85] M.V. Hoffman, Eu^{2+} Emission in ternary alkaline earth aluminum fluorides, J. Electrochem. Soc. 119 (1972) 905, doi:10.1149/1.2404366.

[86] B. Latourrette, F. Guillen, C. Fouassier, Energy transfer from Eu^{2+} to trivalent rare earth ions in BaY_2F_8, Mater. Res. Bull. 14 (1979) 865–868.

[87] G. Blasse, On the Nature of the Eu2+ luminescence, Phys. Status Solidi Basic Res. 131 (1973) 5–8.

[88] W. Zhang, R. Hua, T. Liu, J. Zhao, L. Na, B. Chen, Preparation, photoluminescent properties and luminescent dynamics of $BaAlF_5:Eu^{2+}$ nanophosphors, Mater. Res. Bull. 60 (2014) 247–251, doi:10.1016/j.materresbull.2014.08.039.

[89] H. Wang, M. Li, The ideal strength of gold under uniaxial stress: an ab initio study, J. Phys. Condens. Matter. 22 (2010) 1–6, doi:10.1088/0953-8984/22/29/295405.

[90] S. Mahlik, M. Grinberg, L. Shi, H.J. Seo, Pressure evolution of $LiBaF_3:Eu^{2+}$ luminescence, J. Phys. Condens. Matter. 21 (2009) 8, doi:10.1088/0953-8984/21/23/235603.

[91] R. Hua, J. Yu, H. Jiang, C. Shi, Mild solvothermal synthesis and luminescent properties of the complex fluorides $KMgF_3$:Eu and $KZnF_3$:RE (RE = Eu, Ce), J. Alloys Compd. 432 (2007) 253–257, doi:10.1016/j.jallcom.2006.05.108.

[92] A. Meijerink, Make a comparison between the two isoelectronic, J. Lumin. 55 (1993).

[93] M.V. Hoffman, Alkaline earth aluminum fluoride compounds with Eu^{2+} activation, J. Electrochem. Soc. 118 (1971) 933, doi:10.1149/1.2408227.

[94] A. Ellens, A. Meijerink, G. Blasse, 6I emission and vibronic transitions of Eu^{2+} in $KMgF_3$, J. Lumin. 59 (1994) 293–301, doi:10.1016/0022-2313(94)90056-6.

[95] G. Boulon, J.C. Gacon, D. Trottier, A. Vedrine, Eu^{2+} Luminescence in KY_3F_{10}, Phys. Status Solidi. 93 (1979) 775–779, doi:10.1002/pssb.2220930236.

[96] J.M.P.J. Verstegen, J.L. Sommerdijk, Line emission of $SrBe_2Si_2O_7$:Eu^{2+} and $BaBe_2Si_2O_7$:Eu^{2+}, J. Lumin. 9 (1974) 297–301.

[97] D. Dutczak, T. Jüstel, C. Ronda, A. Meijerink, Eu^{2+} luminescence in strontium aluminates, Phys. Chem. Chem. Phys. 17 (2015) 15236–15249, doi:10.1039/c5cp01095k.

[98] G. Blasse, Thermal quenching of characteristic fluorescence, J. Chem. Phys. 51 (1969) 3529–3530, doi:10.1063/1.1672543.

[99] H. Kuroda, S. Shionoya, T. Kushida, Mechanism and Controlling Factors of Infrared-to-Visible Conversion Process in Er^{3+} and Yb^{3+}-Doped Phosphors, J. Phys. Soc. Japan. 33 (1972) 125–141, doi:10.1143/JPSJ.33.125.

[100] J. Sytsma, K.M. Murdoch, N.M. Edelstein, Spectroscopic studies and crystal–field analysis of Cm^{3+} and Gd^{3+} in $LuPO_4$, Phys. Rev. B. 52 (1995) 668–676.

[101] D.C. Wallace, H. Callen, Thermodynamics of crystals, Am. J. Phys. 40 (1972) 1718–1719, doi:10.1119/1.1987046.

[102] G. Grimvall, B. Magyari-Köpe, K.A.Persson OzoliņENM, Lattice instabilities in metallic elements, Rev. Mod. Phys. 84 (2012) 945–986, doi:10.1103/RevModPhys.84.945.

[103] M. Born, K. Huang, M. Lax, Dynamical Theory of Crystal Lattices, Am. J. Phys. 23 (1955) 474–474, doi:10.1119/1.1934059.

[104] D.C. Wallace, Thermoelasticity of stressed materials and comparison of various elastic constants, Phys. Rev. 162 (1967) 776–789, doi:10.1088/1751-8113/44/8/085201.

[105] Z. Zhou, B. Joós, Stability criteria for homogeneously stressed materials and the calculation of elastic constants, Phys. Rev. B - Condens. Matter Mater. Phys. 54 (1996) 3841–3850, doi:10.1103/PhysRevB.54.3841.

[106] J. Wang, J. Li, S. Yip, S. Phillpot, D. Wolf, Mechanical instabilities of homogeneous crystals, Phys. Rev. B. 52 (1995) 12627–12635, doi:10.1103/PhysRevB.52.12627.

[107] S.V. Rashchenko, A. Kurnosov, L. Dubrovinsky, K.D. Litasov, Revised calibration of the $Sm:SrB_4O_7$ pressure sensor using the Sm-doped yttrium-aluminum garnet primary pressure scale, J. Appl. Phys. 117 (2015) 2–7, doi:10.1063/1.4918304.

[108] F. Datchi, A. Dewaele, P. Loubeyre, R. Letoullec, Y.Le Godec, B. Canny, Optical pressure sensors for high-pressure-high-temperature studies in a diamond anvil cell, High Press. Res 27 (2007) 447–463, doi:10.1080/08957950701659593.

[109] T. Tröster, Optical studies of Non-Metallic compounds under pressure, Handb. Phys. Chem. Rare Earths. 33 (2003) 515–589, doi:10.1016/S0168-1273(02)33007-1.

[110] K.L. Bray, Transition metal and rare earth compounds: excited states, Transitions, Interactions I (2001).

[111] K.A.J. Gschneidner, L. Eyring, Handbook on the physics and chemistry of rare earth, 1986. doi:10.1016/s0925-8388(96)02845-9.

[112] Z. Barandiarán, L. Seijo, Quantum chemical analysis of the bond lengths in fn and f n-1 d1 states of Ce^{3+}, Pr^{3+}, Pa^{4+}, and U^{4+} defects in chloride hosts, J. Chem. Phys. 119 (2003) 3785–3790, doi:10.1063/1.1590952.

[113] R. Valiente, F. Rodríguez, J. González, H.U. Güdel, R. Martín-Rodríguez, L. Nataf, M.N. Sanz-Ortiz, K. Krämer, High pressure optical spectroscopy of Ce^{3+}-doped $Cs_2NaLuCl_6$, Chem. Phys. Lett. 481 (2009) 149–151, doi:10.1016/j.cplett.2009.09.059.

[114] J.L. Pascual, Z. Barandiarán, L. Seijo, Relation between high-pressure spectroscopy and $f^{n-1}d^1$ excited-state geometry: a comparison between theoretical and experimental results in SrF_2: Sm^{2+}, Phys. Rev. B - Condens. Matter Mater. Phys. 76 (2007) 1–6, doi:10.1103/PhysRevB.76.104109.